POLITECNICO DI MILANO

Master of Science in Biomedical Engineering

Department of Electronics, Information and Bioengineering

POLITECNICO
MILANO 1863

SAFETY ENHANCEMENT IN ROBOTIC NEUROSURGERY

Supervisor: Elena De Momi, PhD

Co-Supervisor: Dott. Ing. Sara Moccia

Cameron Riviere, PhD

Thesis of:

Francesca Prudente, identification number 836825

Academic year 2016-2017

Ai miei genitori

Abstract

Microvascular decompression and convexity meningioma resection are known to be among the most technically challenging microneurosurgery procedures. The incidence of associated complications depends on tumour size, surgeon experience and the operative approach chosen. Although several treatments are available, surgery is the gold standard since it reduces patient mortality or after-treatment morbidity. It requires to avoid bleeding and to preserve large vessels and sinuses (i.e. superior sagittal or transverse) in order to improve post-operative outcomes. Indeed, bleeding is well recognized in the clinical literature as one of the most common complications (10.2% out of all cases). It can lead to different kinds of deficit, such as edema, seizures, postoperative haemorrhage, and cerebral ischemia. During surgery, the primary imaging source to obtain a magnified view of both brain and cerebral vessels is microscopy.

Here a list of limitations of current surgery procedures so that the use of a robot is justified:

- The issue to preserve the integrity of the petrosal vein during the microvascular decompression intervention arises in order to avoid cerebral edema and bleeding;

- During convexity meningioma resection neurosurgeons are asked to avoid the contact with the superior sagital sinus, transverse sinus and cortical sur-

rounding veins in close proximity to the tumor.

Several robotic systems have been developed to assist surgeons in microneurosurgery interventions. However, they have not seen widespread clinical use due to drawbacks such as large size, obtrusiveness in the cramped surgical field, inability to adapt to changing conditions, limited function, inadequate integration with existing clinical workflow, increased operative time and high cost. All these issues can be overcome using a completely handheld active instrument to implement avoidance zones and automatic force control. Thus, all the surgeon's training, dexterous manipulation capability, and ability to adapt are retained.

The present work investigates the use of Micron, a robotic handheld tool, to perform vessel avoidance in neurosurgery. The robot, whose position is registered with regard to the patient anatomy, is programmed to avoid entering into certain predefined avoidance zones. These are implemented as forbidden-region virtual fixtures. A geometrical deformable model-based approach is used to perform vessel segmentation. It requires minimum manual intervention, consisting in the selection of two seed points. The evolution of the geometrical deformable model is guided by an intensity-based external force, which is retrieved from *vesselness* measures. Kalman filtering is exploited to track the vessel position between consecutive microscopy frames. The 3D reconstruction is performed using a stereo-microscope in order to extract the 3D position of the vessel surface in the robot control reference system. The control command is triggered as soon as the distance between the tool tip and the vessel becomes lower than a predefined threshold or the tip attempts to enter inside the vessel.

Microscopy videos were recorded during neurosurgery interventions at Istituto Neurologico Carlo Besta (Milan, Italy) and used to asses the reliability of the segmentation and tracking algorithms. Numerical evaluation of vessel segmentation and tracking was performed with respect to the manual segmentation carried out

by an expert, elected as gold standard. The good results obtained (median accuracy= 0.9990) showed the reliability of the segmentation algorithm to extract the vessel boundaries. The tracking algorithm proved to accurately follow the motion of the vessel in the surgical scene (median accuracy = 0.9927).

Phantom vessels were developed in order to test the quality of the 3D reconstruction method and to let Micron interact with them simulating a surgical scenario. The 3D reconstruction method was assessed in terms of spatial errors (median= 0.2960 mm) in order to evaluate quantitatively its accuracy. The vessel avoidance algorithm was tested in real-time by driving the Micron above the phantom vessels and making repeated attempts to cross them. The virtual fixtures evaluation showed that Micron reliably constrains the tool movements into predefined forbidden zones. Indeed, the statistical analysis, performed with Wilcoxon test (significance level = 0.05), revealed that there were statistically significant differences between the controlled trajectory of the Micron tip and the trajectory that would have been if the controller were disabled.

Future work will aim at implementing a tracking algorithm for real-time applications and at developing a 3D phantom that reproduces a more truthful surgical scenario.

Sommario

Tra le procedure di microneurochirurgia tecnicamente più complesse vi sono la decompressione microvascolare per la nevralgia del trigemino e la resezione dei meningioma della convessità. L'incidenza delle relative complicanze è fortemente legata a diversi fattori, quali le dimensioni del tumore, l'esperienza del chirurgo e il tipo di approccio scelto. Nonostante siano presenti diversi tipi di trattamento, la chirurgia rimane il *gold standard* in quanto garantisce risultati migliori nel post-operatorio e riduce i danni che possono portare alla morte del paziente. Tuttavia, si rende necessario minimizzare i rischi dovuti a gravi emorragie preservando l'integrità dei grandi vasi e dei seni venosi della dura madre (sagittale superiore e trasverso). È stato evidenziato che le complicazioni più comuni in neurochirurgia sono legate ad eccessive emorragie che possono causare deficit di diverso tipo e calibro. La soluzione tecnologica comunemente impiegata dai neurochirughi è la microscopia che offre un'ottima e chiara visualizzazione del campo operatorio.

Nel corso degli ultimi decenni sono stati sviluppati diversi sistemi robotici con l'obiettivo di ridurre l'invasività delle procedure neurochirurgiche. Il successo riscontrato da questi robot in sala operatoria è rimasto piuttosto contenuto a causa di importanti limiti: grandi dimensioni, ingombro eccessivo, scarsa versatilità, costi elevati e difficoltà di integrazione nel workflow chirurgico standard. L'alternativa è utilizzare un dispositivo completamente *handheld* in modo che il chirurgo possa manipolare direttamente i tessuti e gestire facilmente eventuali

situazioni inattese.

L'obiettivo del presente lavoro di tesi è quello di implementare un algoritmo di *vessel avoidance*, o *forbidden-region virtual fixtures*, in modo da limitare i movimenti di un *tool handheld*, in specifiche regioni dello spazio. Per inviduare la posizione della struttura vascolare di interesse si è ritenuto necessario segmentare il vaso in immagini acquisite da uno stereomicroscopio chirurgico. L'algoritmo di segmentazione vascolare, basato su un modello geometrico deformabile, viene inizializzato attraverso la selezione manuale di due punti che definiscono le estremità del vaso, dopodiché procede automaticamente fino ad estrarne i contorni. Il tracking vascolare in frame video successivi è stato realizzato off line sfruttando la predizione del filtraggio di Kalman. Una volta ricostruito il volume del vaso e ricavate le sue coordinate spaziali nel sistema di controllo del robot, l'algoritmo di *vessel avoidance* impone il rispetto di una distanza di sicurezza tra l'end effector del tool e la superficie vascolare.

Il materiale digitale per il lavoro, ovvero video registrati al microscopio durante due interventi di neurochirurgia, è stato gentilmente fornito dall'Istituto Neurologico C. Besta di Milano (Italia) e l'algoritmo è stato implementato per controllare il Micron, un *tool* robotico per microchirurgia sviluppato alla Carnegie Mellon University, Pittsburgh (Pennsylvania, USA). Per verificare l'applicabilità dell'algoritmo di ricostruzione 3D e di *virtual fixtures* è stato sviluppato un set-up sperimentale per simulare l'ambiente chirurgico e permettere al Micron di interagire con vasi fantoccio.

La validazione dell'algoritmo di segmentazione e tracking vascolare è stata effettuata confrontando i risultati ottenuti con quelli della segmentazione manuale, eseguita da un esperto, scelta come *gold standard*. Gli ottimi risultati ottenuti (mediana dell'accuratezza= 0.9990) hanno confermato l'affidabilità dell'algortimo di segmentazione vascolare. La valutazione dell'algortimo di tracking ha dimostrato

che il metodo é in grado di seguire accuratamente il movimento del vaso in frame video successivi (mediana dell'accuratezza= 0.9927). Per valutare la qualità della ricostruzione 3D sono stati calcolati i valori degli errori spaziali in mm (mediana=0.2960). L'analisi delle performance dell'algoritmo di *virtual fixtures* in real–time ha dimostrato che l'algoritmo è in grado di preservare l'integrità di strutture critiche quali vasi, limitando i movimenti del chirurgo durante l'operazione in maniera affidabile. L'analisi statistica eseguita con un test di Wilcoxon (livello di significatività= 0.05) ha rivelato che ci sono differenze statistiche significative tra la traiettoria del Micron con controllo e quella che avrebbe percorso il Micron se non fosse stato controllato.

Possibili sviluppi futuri riguardano il miglioramento dell'algoritmo di tracking per applicazioni real-time in modo da tenere in considerazione la deformazione dei tessuti e la presenza di strumenti chirurgici che potrebbero occludere il vaso. Infine, si potrebbe realizzare un fantoccio 3D in modo da riprodurre uno scenario chirurgico più simile a quello reale per le analisi in laboratorio.

Acknowledgements

This thesis could not have been possible without the assistance and help of many people that I would like to acknowledge.

First of all, I want to express my gratitude to my supervisor prof. Elena De Momi for her mentorship, guidance, faith in me and for always urging me to do better. I am particularly grateful to my co-supervisor Sara Moccia for being such a source of encouragement and inspiration to me on an academic and personal level. I sincerely appreciate her extreme patience, hard work, consistent support, expertise, generosity and willingness to spend her valuable time on me. I also greatly thank my second co-supervisor prof. Cameron Riviere who gave me the chance to work in his laboratory and pursue my research in the United States. His dedication, interest and above all his attitude to motivate students helped me complete my work.

I wish to express my thanks to Dr. Alessandro Perin for providing me with the surgical knowledge and material necessary for the research and for letting me enter in the operating room.

My biggest thanks go to my parents because they always believe in me more than I do. I am grateful to Paola and Benedetta for our true unique and priceless friendship. Many thanks to all the friends that I met in Pittsburgh with whom I shared joy and struggles and who made me feel at home on the other side of the world.

Contents

List of Figures

List of Tables

Chapter 1

Introduction

1.1 Clinical background

In neurosurgery surgeons have to perform minute and accurate operations with poor visibility due to blood and CerebroSpinal Fluid (CSF) [7]. Intra-operative navigation supports surgeons in performing these tasks ensuring safer and more precise gestures.

Surgical Navigation Systems (SNS) provide an accurate surgical guidance empowering surgeons to make decision in the operating room tracking precisely surgical tools in relation to patient anatomy. This technology provides instantaneous localization information integrating 3D imaging data of the surgical planning with instrument tracking and intra-operative imaging technologies [49]. Contemporary advanced SNS are able to provide real-time information about instrument location, orientation and relationship to nearby structures, usually exploiting multimodal imaging.

This work is focused on MicroVascular Decompression (MVD) and Convexity Meningiomas (CM) resection, which are taken as benchmark because they are known to be among the most technically challenging microneurosurgery proce-

dures [27, 56]. In particular the study aims at investigating the use of a robotic handheld system to perform vessel avoidance, a critical aspect explained in detail in Sec. 1.1.2 and Sec. 1.1.4.

1.1.1 Trigeminal neuralgia

Trigeminal neuralgia is a chronic condition affecting the trigeminal nerve that causes extreme, sporadic, sudden burning or shock-like facial pain. The trigeminal nerve, also known as the the fifth (V) cranial nerve, arises from the brainstem and it is divided into three branches (Fig. 1.1):

1. Ophthalmic division (V1 in Fig. 1.1) that supplies sensation to the forehead and eye;

2. Maxillary division (V2 in Fig. 1.1) that provides sensation to the cheek, upper lip, and roof of the mouth;

3. Mandibular division (V3 in Fig. 1.1) that provides sensation to the jaw and lower lip; it also supplies movement of the muscles involved in biting, chewing, and swallowing.

Trigeminal neuralgia is caused by an abnormal compression of the trigeminal nerve, either by an artery or a vein and it mainly occurs in the cerebellopontine angle at the root entry/exit zone nearby the brainstem [19]. The main offending vessels are the superior cerebellar artery or a branch of the petrosal vein. Although the exact incidence is unknown, in the US approximately 10,000 to 15,000 cases are diagnosed each year. The average incidence of trigeminal neuralgia is 4,3 per 100,000 people per year; it affects more probably women (5,9/100,000) than men (3,4/100,000) [47].

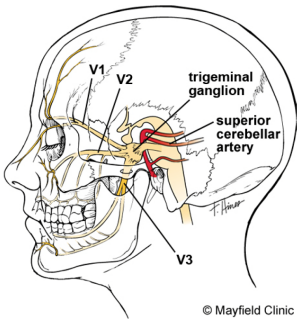

Figure 1.1: Superior cerebellar artery compressing trigeminal ganglion, the sensory ganglion of the trigeminal nerve. The trigeminal nerve is divided in three branches: the ophtalmic division (V1) that provides sensation to the forehead and eye, the maxillary division (V2) that supplies sensation to the cheek, upper lip and mouth roof and the mandibular division (V3) that provides sensation to the jaw and the lower lip.

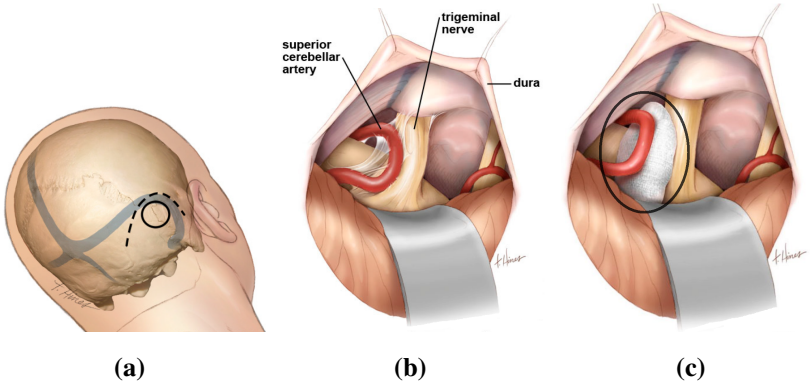

Figure 1.2: Microvascular decompression. (a) A skin incision made behind the ear (dashed line) and a 1-inch craniectomy (solid line) made in the skull. (b) The superior cerebellar artery compressing the trigeminal nerve causing trigeminal neuralgia. (c) The black circle indicating the sponge inserted between the nerve and the blood vessel.

1.1.2 Trigeminal neuralgia surgery

Several neurosurgical procedures are available to treat trigeminal neuralgia, such us balloon compression, glycerol injection, stereotactic radiofrequency rhizotomy, stereotactic radiosurgery and MVD.

Balloon compression seems to be suitable for patients who have V1 pain and are not good candidates for MVD. Alternatively these patients can undergo other procedures including glycerol rhizotomy, peripheral nerve section, and radiosurgery. However, balloon compression carries the highest risk of postoperative trigeminal motor weakness.

Patients who have pain over V1 or the entire face and cannot undergo a posterior fossa procedure are good candidates for glycerol rhizotomy. The main advantage of glycerol rhizotomy is the low risk of postoperative trigeminal motor complications so it is particularly indicated for patients with contralateral pain, trigeminal motor weakness, and temporomandibular joint dysfunction.

Radiosurgery can be the best solution in the treatment of patients who, for instance, are taking anticoagulants and cannot receive a surgical intervention. Percutaneous destructive procedures such as stereotactic radiofrequency rhizotomy can be recommended for patients in poor medical conditions because it reduces the risk of dysesthesias. It is not suitable for patients with V1 pain and pain spread over the three trigeminal divisions.

Since the risk of pain recurrence, dysesthesia, corneal analgesia and trigeminal motor weakness is very low, MVD has become a very successful and widespread technique. However, it is not appropriated for patients in poor medical condition, with contralateral hearing loss or with large and ectactic arterial system due to the high perioperative morbidity.

All the existing surgical procedures are related to the risk of pain recurrence but many studies have shown that the outcomes obtained with MVD and percu-

Anatomical checkpoints	Imaging modalities
Skull morphometry and extent of mastoid hair cells	X-ray, CT, MRI
Surface landmarks for the junction of the transverse and sigmoid sinuses	CT
Presence of the subdural spaces and width of the cerebellopontine cistern	MRI
Position of the superior petrosal vein in the mediolateral aspect	CT, MRI
Identification of the vessel(s) compressing the trigeminal nerve	MRI

Table 1.1: Anatomical checkpoints for microvascular decompression planning and imaging modality required to recognize the checkpoints.

taneous stereotactic radiofrequency rhizotomy lead to the highest long-term pain relief [1]. Therefore one of the most effective procedure is the MVD [19]. MVD requires to insert a tiny teflon sponge to separate the compressed nerve from the compressing blood vessel (Fig. 1.2).

Surgical planning

In the MVD planning phase, patients usually undergo imaging examinations, such as X-ray, Computed Tomography (CT), Magnetic Resonance Imaging (MRI) and angiography, in order to both get morphometric information of the neurovascular structures and define anatomical checkpoints [29]. Commonly adopted imaging modalities require to recognize checkpoints that are shown in Tab. 1.1.

MRI is able to scan neuronal tissue, cranial nerves and vascular structures within the posterior fossa with the highest resolution (1mm) with respect to the other imaging techniques. In this contest the T2 weighted Constructive Interfer-

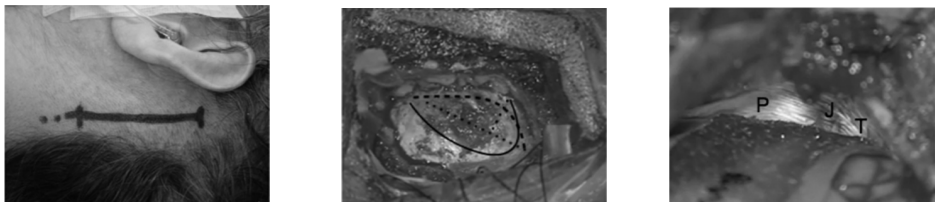

(a) **(b)** **(c)**

Figure 1.3: Craniotomy for microvascular decompression. (a) Curved linear skin incision. (b) U-, T- or -L shaped dural incision along the venous sinus. (c) Petrous dura (point P), tentorium (point T) dura and petrotentorial junction (point J) landmarks for craniotomy.

Figure 1.4: The DORO LUNA® Brain Retractor System is shown.

ence in Steady State (CISS) MRI turned out to be the most suitable because it reveals high contrast between the vascular structures and the CSF. The CSF is mapped to high intensity values whereas the enclosed target vessels and nerves are reproduced with low signals.

At Istituto Neurologico Carlo Besta planning is performed using the three-dimensional (3D) CISS MRI which is a gradient-echo MRI sequence.

Surgical procedure

MVD is performed under general anesthesia, and with the patient in the lateral decubitus position with the head and the trunk turned to the contralateral side. The skin incision can be either linear (Fig. 1.3a) or curved linear, and its center is in correspondence of the mastoid notch. The craniotomy is performed to expose

the transverse and sigmoid sinuses but avoiding sinus injury. The dural incision can be *U*-, *T*- or *L*-shaped along the venous sinus (Fig. 1.3b). The first intradural landmarks are the petrous dura, tentorium, and petrotentorial junction (Fig. 1.3c). Once the dura is opened, the cerebrospinal fluid is drained. After the craniectomy and dural opening, surgeons use a brain retractor (Fig. 1.4) placed at the edge of the petrotentorial junction to avoid cerebellum compression. It is preferable to preserve the petrosal vein since its closure has been linked to cerebral edema and bleeding.

Commonly, MVD requires to interpose a soft cushion between the superior cerebellar artery or a branch of the petrosal vein and the trigeminal nerve. The procedure is made of two main steps:

1. The artery is outstripped from the original compression site and fixed to the tentorial surface with fibrin glue;

2. The cushion is interposed.

The cushion can be built with different materials: teflon, ivaron, polyurethane sponge, silicone sponge, vascular tape, fibrin glue and collagen sheet [29].

During the surgical intervention, neurosurgeons normally use both microscope and endoscope to visualize the brain and to provide a high magnification (2.5X to 25X).

Additionally, image-based SNS can be employed, as demonstrated in [19, 37]. One of the several advantages brought by SNS to MVD is to identify the full spatial extent of the cranial nerve-compressing vessel interface. Besides this, it allows to optimize the craniectomy localization.

Risks and percentage of failure

The most common complication in cerebrovascular surgery is bleeding requiring transfusion whose incidence is the 10.2% [41]. It can lead to different kinds of deficit, such as edema, seizures, postoperative haemorrhage and cerebral ischemia. Other risks related to MVD include incisional infection (1.3%), facial palsy (2.9%), cerebrospinal fluid leak (1.6%), dysesthesia (5%) [70] and postoperative mortality whose incidence is 0.1%. Trigeminal nerve damage can lead to hearing loss ($<$1%), facial numbness (9.1%) or paralysis (0.15%) [1].

1.1.3 Meningioma

Meningiomas are a common type of primary intracranial neuroplasm that arises slowly from the middle layer of the meninges, the arachnoid within the thin, spider-web like membrane covering the brain and the spinal cord. Different kinds of meningiomas can be distinguished depending on their location [49]:

- Convexity Meningiomas (CM);
- Parasagittal and falcine meningiomas;
- Tentorial meningiomas;
- Skull base meningiomas;
- Anterior skull base meningiomas;
- Middle and posterior skull base meningiomas;
- Intraventricular meningiomas;
- Pineal region meningiomas.

The incidence of pathologically-confirmed meningioma is estimated to be approximately 97.5/100,000 per year in the US [68]. The most common meningioma is the CM, which represents the 20% of all cases. CMs grow on the surface of brain directly under the skull, toward the convexity.

Since meningiomas usually grow slowly, they may reach large size before patient starts experiencing symptoms, which moreover depend on the meningioma location and extent. Symptoms may include headache (due to the change of the pressure level in the brain, meningioma can cause confusion, difficult in focusing and sometimes can be associated to nausea or vomiting), seizures (such as epilepsy, muscle spasm and visual hallucinations) neurological deficits (especially if meningioma originates near the motor and sensory areas) and vertigo.

1.1.4 Meningioma surgery

Meningioma treatment options include surgery, radiation therapy and chemiotherapy. Surgery is the gold standard since it offers the best chance for a cure [2]. During the surgical procedure, stereotactic imaging and instrument guiding systems allow neurosurgeons to perform brain navigation. Stereotactic neurosurgery is a minimally invasive technique which employs a 3D coordinate system to locate targets inside the body. It makes use of a computer system that integrates previously obtained imaging (usually CT or MRI) and provides a 3D representation of the brain in order to guide the surgeon during the lesion removal.

Surgical planning

Advanced imaging techniques can be used to diagnose the presence of the tumor but also to plan meningioma surgery. CT (Fig. 1.5a) and MRI (Fig. 1.5b) are commonly adopted. Meningiomas are mainly isodense with the grey matter in T1-weighted MRI, and hypointense or hyperintense in T2-weighted MRI. In

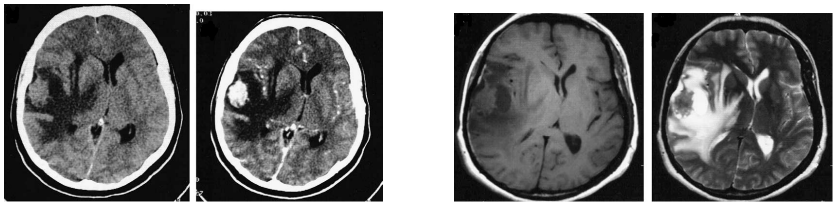

(a) **(b)**

Figure 1.5: Meningioma imaging. (a) Computerized tomography. (b) Magnetic resonance (T1-weighted MRI on the left, T2-weighted MRI on the right).

most cases, meningiomas appear hyperdense on CT scans and sometimes they can be calcified. The most effective technique to identify the correct tumor localization is the contrast-enhanced MRI [3]. Magnetic Resonance Angiography and arteriogram may be performed if embolization is needed. Embolization, which obstructs the blood vessel flow to the meningioma with a glue, is required in case of tumors with an extensive blood supply to prevent from excessive bleeding during surgery [4]. Magnetic Resonance Spectroscopy is useful to define the tumor chemical characteristics and determine the nature of the lesions seen on the MRI.

For integration in SNS, conventional MRI and vascular imaging, as Magnetic Resonance Venography and Angiography, are usually used since they allow identifying underlying nerves, vascular structures and cortical anatomy. Generally, for CM, MRI is the principal modality integrated in the SNS.

Surgical procedure

CM are the easiest to access with respect to other meningiomas, due to their superficial location in the brain [5].

The constant principle in meningioma removal is the following: if possible, all involved or hyperostotic bone should be resected. The dura involved by the tumor as well as a dural rim that is free from tumor should be removed. Thus, CM surgery provides for a complete macroscopic resection, including dural adherence

and any involved bony structures [45]. In order to completely remove the tumoral mass, the resection is performed considering a 5 mm dural margin. Ultrasonic aspirators can be used to dissect and aspirate out parts of the tumoral mass.

SNS allows targeting linear skin incision, optimizing the size of the craniotomy and localizing important structures the surgeon wants to avoid, such as arterial or venous structures and nerves [56]. Better-centered craniotomies have some advantages: reduced blood loss, decreased operating time and minimization of trauma and brain retraction, consequently reducing the risk of post-operative swelling and/or hematomas. Surgical intervention planning implies three steps:

1. Patient positioning;
2. Registration;
3. Definition of the trajectory.

A SNS for meningiomas was developed by Omay et al. [49] (Fig. 1.6). Using *oblique* displays containing the axis of the pointing tool and images perpendicular to this axis is the most common approach. Perpendicular display helps the surgeon get aware of the relative positions of superior sagital sinus, transverse sinus and cortical surrounding veins.

Risks and percentages of failures

Sparing brain vessels is vital in order to achieve a good surgical outcome. In particular: brain arteries and veins must be preserved to avoid a stroke or a venous infarction respectively. On the other hand, large sinuses (i.e. superior sagittal or transverse sinus) when ruptured or torn apart might cause major bleedings that can be lethal for the patient. Other complications may include seizures, wound infection (3.5%), deep venous thrombosis requiring anticoagulation (4.2%), epidural hematoma requiring evacuation (1.4%) and CSF leakage (1.4%) [56].

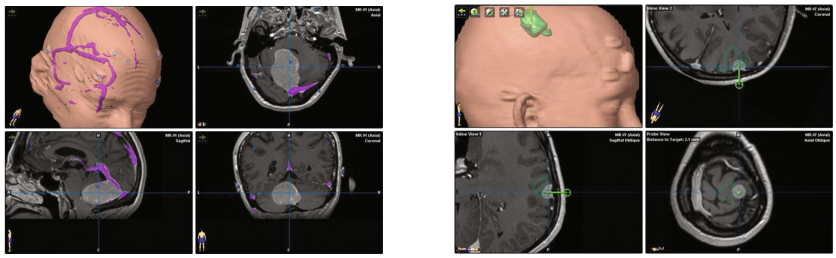

(a) **(b)**

Figure 1.6: Surgical navigation system interface. (a) High-resolution MRI (grayscale) with enhanced vascular anatomy (render in violet) (b) Tumoral mass of a convexity meningioma using oblique display. fMRI provides functional/anatomical information that allows to determine the tumor location (green) with respect to the superial sagittal sinus and nearby cortical veins.

1.2 General objectives

Improvements in microsurgical dissection techniques, skull base approaches, imaging modalities, and intraoperative neurophysiologic monitoring have led to a reduction in surgical morbidity and mortality for brain tumors and cerebrovascular lesions. Despite these improvements, postoperative rates of cerebral infarction and cranial nerve deficits remain high and dramatically reduce quality of life in patients with a variety of brain disorders [36], [57]. Moreover, bleeding requiring transfusion is well recognized in the clinical literature as one of the most common complications (10.2% out of all cases) [41]. According to the percentage values of risks and failures, reported in Sec. 1.1.2 and Sec. 1.1.4, nerves, vessels and sinuses preservation are of primary importance during neurosurgery interventions, since they strongly influence surgical outcomes. Injuries of the cranial nerves and blood vessels that may occur during the surgical procedure have been related to misplacement of surgical tools with respect to the structures of interest [69, 9].

An assist device that would allow the surgeon to reduce larger unintended movements of the human hand would result in reduced morbidity for patients. The objective of the present work is to perform vessel and nerve collision avoid-

ance using a fully handheld robotic tool. In order to address this issue a vascular segmentation algorithm was developed that is able to derive avoidance zones, such as vessels and nerves, from patient's anatomy under a surgical stereomicroscope. The vessel tracking in consecutive video frames was implemented exploiting Kalman filtering prediction in order to determine the vessel position over time.

Preliminary results were presented in "Safety enhancement in robotic neurosurgery through vessel tracking" S. Moccia, F. Prudente, E. De Momi, C. Riviere, A. Perin, R. Sekula, L.S. Mattos (CRAS conference, 2016) [44]. The analysis of the segmentation and tracking algorithms on videos recorded during real surgeries showed the method to be effective and robust. However, the paper only describes an algorithm to extract and enhance vessel contours in order to provide a visual support to neurosurgeons during micromanipulation.

The present work, instead, aims at providing a concrete technical support to surgeons by commanding a robotic tool to deflect its own tip when it comes within a safety distance with respect to the target vessel. The safety distance range chosen is 1-2 mm, as suggested in [67]. The system is supposed to enhance safety preventing injuries that may lead to postoperative complications. The method presented in S. Moccia et al. [44] is exploited but further developments are proposed. Once the system has been calibrated, 3D reconstruction techniques are applied in order to retrieve the spatial coordinates defining the position and the orientation of vessel volume in the 3D world. Micron real-time tracking system enables to locate in every moment the tool's tip with respect to the avoidance zones in order to trigger the control when it is necessary. Thus, the work can be divided in the following parts:

- Segmentation algorithm (Sec. 3.1)
- Inter-frame tracking (Sec. 3.2)

- 3D reconstruction (Sec. 3.3)
- Virtual fixtures (Sec. 3.4)

Chapter 2

State of the art

2.1 Vessel segmentation and tracking

Segmentation of tubular structures is a problem that arises in many clinical applications mostly to detect anatomical surfaces of blood vessels in medical images. The main studies in this field have been focused on identifying vessels within preoperative images in order to derive the optimal surgical plan. Nowadays, a large literature on vessel segmentation and tracking algorithms exists and a recent review can be found in [22], where algorithms are divided in:

- Pattern recognition techniques;
- Matched filtering;
- Vessel tracking/tracing;
- Morphological processing;
- Multiscale approaches;
- Model based approaches.

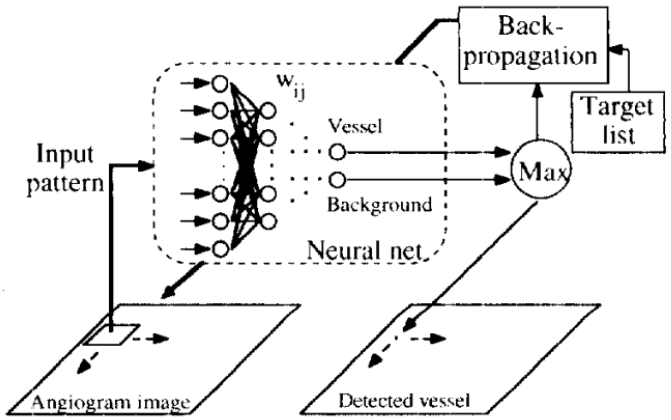

Figure 2.1: Architecture of the multilayer feed-forward network window classifier. The gray-scale values of a square region of the histogram are sent to the input units. The network training is performed applying the back-propagation algorithm on the target list points. The state of the output units allows to segment the vascular structure by distinguishing the vessel from the background.

In vessel segmentation algorithms, the input image normally must be pre-processed so it undergoes noise suppression, data normalization, contrast enhancement and conversion of color image to grayscale image.

2.1.1 Pattern recognition techniques

The algorithms based on pattern recognition work on the automatic detection of pixels belonging to vessels and the ones belonging to the background. They can be classified in two cathegories: supervised techniques and unsupervised techniques. The former deals with prior labeling knowledge to establish how to classify pixels whereas the latter does not exploit this prior information.

Supervised methods

The learning rule for vessel segmentation in supervised methods is found by the algorithms relying on a training set of manually segmented reference images, con-

sidered as Gold Standard (GS). The segmentation is performed normally by an expert observer. In order to establish a classification criterion a ground truth dataset of determined features should be available. Since they work on pre-segmented data the supervised algorithms can produce more reliable results with respect to unsupervised techniques. They use neural networks whose mathematical weights correspond to the probability of input data to give a specified output. The network is trained with labeled data (data whose output is known) and can have a feedback system. Nekovei and Ying et al. [46] developped a neural network classifier trained using a back-propagation algorithm for vascular structures detection in angiography (Fig.2.1). The classification of the center pixel is obtained exploiting the gray-scale information within a multilayer feed-forward network window. It does not require a priori feature extraction because the network is directly applied to angiogram pixels.

Unsupervised methods

The unsupervised class of machine learning approaches is able to build a model that can detect hidden features from the input image. The use of such methods is justified by the absence of GS. Oliveira et al. [48] proposed a method to perform liver vessel segmentation based on region-growing in CT images. A pixel is included in the growing region if its intensity belongs to a predefined range of values. The image histogram is approximated by only three Gaussians through Gaussian Mixture Model [20], where the Gaussian at higher intensities are related to vessel pixel intensities. This approximation allows to determine the range extrema. Feng et al. [71] implemented an analogous method to segment brain vessels. This method differs from the previous one because of the use of the Maximum Intensity Projection (MIP) version of the CT (Fig.2.2a). Since the MIP enhances the contrast between vessel pattern and the background they considered

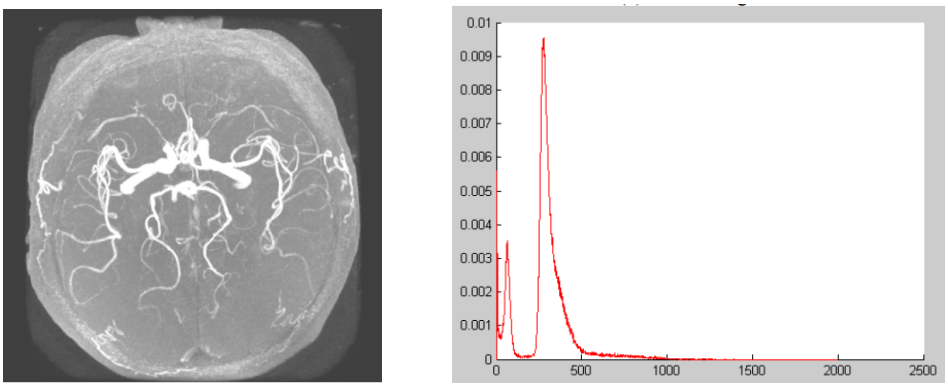

(a) **(b)**

Figure 2.2: Brain vessel segmentation on MRI images using a Gaussian Mixture Model. (a) Maximum Intensity Projection (MIP) used as a preprocessing step to enhance vessels. (b) MIP-Histogram.

only two classes of values in the MIP-histogram approximation (Fig. 2.2b).

2.1.2 Matched filtering

Vessel segmentation performed by Matched Filtering (MF) techniques implies the convolution of a 2-D kernel with the image of interest. The kernel models a feature whose position and orientation in the image are not known in advance. It represents a sort of template designed to replicate features of the structures of interest, such as shape and intensity. Correlation values between the MF and the image are high where such features are encountered.

It is necessary to make two considerations:

- Vessels are piecewise linear because they have an elongated structures with limited curvature;
- Vessel cross-section intensity can be approximated as Gaussian-shaped whose standard deviation is proportional to the vessel thickness. The second as-

sumption requires to consider a filters' family with different standard deviations σ that can be able to detect varying thickness vessels.

Chaudhuri et al. [15] used the convolution of a 2-D linear kernel with a Gaussian profile in order to segment retinal vessels. Since blood vessel typically has a Gaussian or a Gaussian derivative shape curve the filter's shape is constructed matching the profile of a blood vessel. In order to solve the issue of fitting into vessels with different orientations the kernel is rotated in 15° increments. Filtering produces different responses and the highest ones are selected for each pixel. Thresholding allows to obtain a binary vessel image. The MF kernel (K_{MF}) is defined as:

$$K(x, y, \theta) = 1/(\sqrt{2\Pi\sigma}\exp(-x'^2/(2\sigma^2) - m \tag{2.1}$$

The linear combination of basis filters produces steerable filters [23] (i.e. a filter with arbitrary orientation). This class of filter is applied in only two basic directions and the response is computed in other directions as a result of the combination of the responses from these two directions. The main advantages of this approach is the faster computation and a high accuracy.

2.1.3 Vessel tracking

Vessel tracking algorithms rely on the selection of seed points and are guided by local image information of single vessels rather than of the whole vasculature pattern. Tracking means following vessel center lines giving information on vessel structure such as branching and connectivity [22]. Seed points can be either manually selected or obtained through vessel enhancement approaches. Since vessels or vessel branches with not defined seed point can not be extraced, tracking approaches are mainly useful to segment connected vascular trees, since the segmentation can be performed with few seed points. Kelvin et al. [52] proposed

a semi–automated method that combines the multiscale vesselness filtering with conventional Livewire framework [11]. Dijkstra's algorithm allows to connect sparse seed points along the vessel boundaries in order to obtain optimal contours. The cost function set includes Frangi's multiscale vesselness measure [21], vessel direction consistency, the edge evidence and the spatial and radius smoothness constraints.

2.1.4 Morphological processing

Morphological image processing is a set of techniques that apply structuring elements to digital images. The two main morphological operators are *dilation* and *erosion*. *Dilation* works on filling empty spaces and connecting disjoint objects whereas *Erosion* shrinks structures. *Closing* is a *dilation* followed by an *erosion* and *opening* is an *erosion* followed by a *dilation*. In medical image segmentation the two most used algorithms based on mathematical morphology are *top hat* and *watershed* transformations. *Top hat* transformation produces an enhancement effect of vessels through the use of a morphology opening. It estimates the local background which is subtracted from the image. A Difference of Offset Gaussian filter combined with multiscale morphological reconstruction is applied to detect vessels [40]. Once the centerlines are extracted, they are enhanced with a modified *top hat* operator with circular structural elements of different dimensions. A morphological reconstruction with a double threshold operator produces binary maps of the vessels obtained at four scales. Then, an iterative seeded region growing process of the centerline image with the set of four binary maps is used to produce the final segmented image. Yang et al. [73] proposed an automatic hybrid method based on the combination of mathematical morphology and a fuzzy clustering algorithm. A morphological top-hat operation removes the background in order to detect blood vessels then vessel extraction is obtained by fuzzy clustering.

2.1.5 Multiscale approaches

A blood vessel can be seen as a structure with a Gaussian like shape cross-section profile, piecewise connected and locally linear, with a gradually decreasing width. Frangi et al. [21] designed an enhancement filter through the computation of the Hessian of an image, the multiscale second order local structure. The eigenvalues of the Hessian are extracted to determine the principal directions in which the local second order structure of the image can be decomposed. It permits directly to find out the direction of the smallest curvature along the vessel pattern. They determined the final vesselness measure using two gray-level invariant geometric ratios computed on the basis of eigenvalues and the Frobenius norm matrix. The main advantage of this approach is the simultaneous noise and background suppression.

2.1.6 Model-based approaches

Model-based tracking approaches aim at tracking vessels according to a pre-defined vascular model in 3D volumes. They can be divided in 2 classes:

- Vessel profile models;
- Deformable models.

The vessel cross-sectional intensity profiles can be seen as an approximation of a Gaussian shape or other profiles like the second-order derivative Gaussian, the cubic spline, or Hermite polynomial profile. The model employed can adopt a lot of shapes; the most used is cylinder with elliptical or circular section. The starting position and orientation of the model is found selecting a seed and estimating the vessel direction in the seed manually or automatically, exploiting enhancement approaches such as matched filtering, vesselness approaches, wavelet approaches,

diffusion filtering. The algorithm, at each step, looks for the best match between the model itself and the image data in the current model neighborhood in order to find the next local orientation and position. Matching between the image and the template can be investigated on the basis of several image-derived features, such us intensity or gradient flux. The deformable models approaches for vessel segmentation can be further classified into two categories:

- Parametric deformable models;
- Geometric deformable models.

The first category includes active contour models, also known as snakes. Segmentation is obtained under the influence of internal (smoothing) forces within the curve itself that produce tension and stiffness and external forces determined by the image features. Snakes work on fitting to on object boundary or other desired structures minimizing an energy state. The main advantage is that they are self adapting and can track dynamic objects. The main issues are that they can only consider edge information and they need an initialization closed to the features of interest in order to avoid local minima.

Geometric models typically rely on the Level Set (LS)-based numerical techniques implemented on the theory of curve evolution geometric flows. The LS method performs the numerical computations involving curves and surfaces on a fixed Cartesian grid with no need to parameterize the objects. Lathen et al. [33] used a LS propagation with local phase information to extract the boundaries of vessels. The local phase, derived using quadrature filters, permits to extract lines and edges in an image. The quadrature filter is defined by a complex pair: the real part consists of a line filter and the imaginary part corresponds to an edge filter. The magnitude of the filter response indicates the signal ”energy” of the detected object whereas the angle (the local phase θ) allows to discriminate between edges

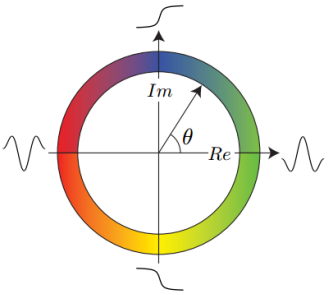

(a)

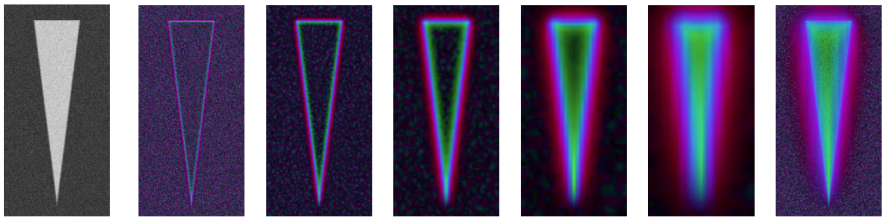

(a) Input (b) Scale 1 (c) Scale 2 (d) Scale 3 (e) Scale 4 (f) Scale 5 (g) Result

(b)

Figure 2.3: Phase-based level set method to segment blood vessels. (a) Quadrature filter implemented as a complex pair where the real part represents the line filter and the imaginary part the edge filter. The angle θ refers to the local phase. (b) Filter responses for increasing scales.

and line (Fig. 2.3a). They also includ multiple scales (Fig. 2.3b) and capture information about vessels of varying width. The resulting ”global” phase is used to drive a contour robustly towards the vessel edges.

2.1.7 Applications in neurosurgery

The approach suggested in [37] is to use implicit segmentation based on volume rendering. First of all it is useful to reduce noise applying anisotropic diffusion in order to provide more homogeneous areas while preserving boundaries. Morphological filtering with 3D gray-value closing operation is exploited to segment the CSF volume. Afterwards, the filter removes the vessels and the nerves correspond-

ing to low intensity values within the CSF volume. In the ”closed” CSF volume the defined boundaries can be extracted using a spherical filter kernel which has to be smaller than the surrounding structures and bigger than the target vessels and nerves. A volume growing technique is performed in order to extract the CSF volume. The use of bounding boxes and the choice to proceed stepwise make the procedure more robust. The segmented ”closed” CSF volume is exploited as a mask to label the original MR data for volume rendering. The last step is the manual labeling of the vessels and the nerves which is performed by a neurosurgeon since requires a deep anatomical knowledge.

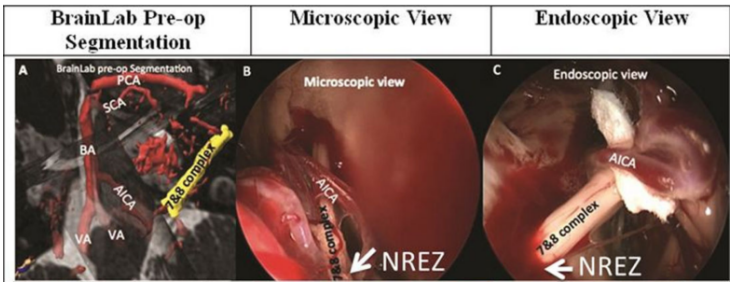

Figure 2.4: BrainLab intraoperative navigation system: preoperative segmentation, microscopic view and endoscopic view.

Dolati *et al.* [19] developed an intra-operative neuronavigation system called *BrainLab iPlanNet*(BrainLab AG, Munich, Germany) able to fuse imaging sequences for segmentation and preoperative planning. The aim of the study was to assess the accuracy of image-based pre-operative segmentation using the gold standard endoscopic and microscopic findings. Individual segmentation of the involved structures was applied by a neurosurgeon and was validated intra-operatively. Pre-operative identification and localization of offending nerves and compressed vessels were compared with the microscopic and endoscopic findings by two blinded neurosurgeons as shown in Fig. 2.4.

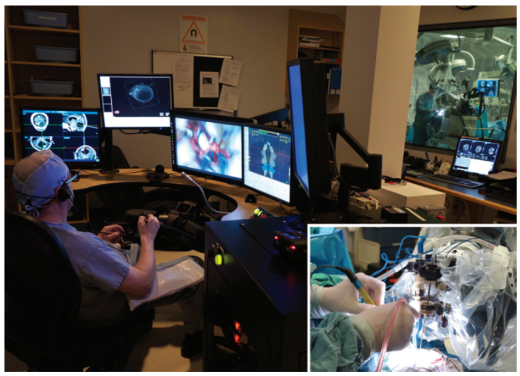

Figure 2.5: The *NeuroArm* system during a surgical intervention in the operating room. The main picture depicts the workstation where the surgeon commands the haptic hand controllers. The inset displays the *neuroArm* manipulators and the assistant surgeon while resecting the tumor.

2.2 Robotic neurosurgery overview

The need of monitoring important cortical structures such as nerves and vessels lead to the development of advanced technologies, based on predictive models and video images integrated in the operating microscope, which are able to face this phenomenon in real time. Different technical methods, either automatic or semi-automatic, have been developed in the last years, but the most common approach has been the master–slave teleoperation [62, 50].

In master-slave surgical systems the operation site is designed as master and the surgical site as slave. This system provides the scaling of the master and the slave manipulator motions in order to perform micro-manipulation [55]. The concept of active constraints is a demanding task for these robots.

The *NeuroArm* system is an image–guided robot that is is made up of two elements: 2MRI–compatible manipulators with 7 degrees of freedom and a work-station provided with a human machine interface that allows to visualize MRI images and real–time high–definition 3D images of the surgical workspace (Fig. 2.5). The *NeuroArm* manipulators are able to handle a wide range of surgical tools [61].

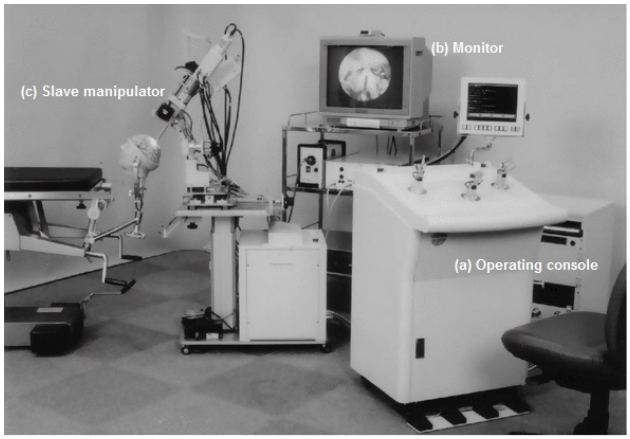

Figure 2.6: The *NeuRobot* system is a tele-controlled micromanipulator developed for invasive neurosurgery. The picture shows: (a) the operating console with three levers on the operation-input device, (b) the 3D monitor connected to the neuroendoscope, (c) the slave manipulator with a tubular cylinder and three microinstruments.

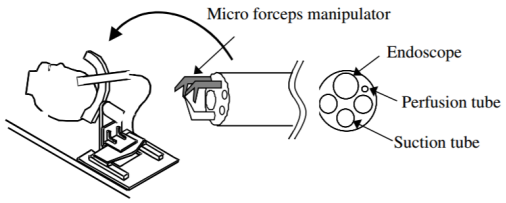

Figure 2.7: The HUMAN is a multifunction system for MRI image guided neurosurgery. The micromanipulator is equipped with two micro forceps manipulator, an endoscope, a suction tube and a perfusion tube integrated in a tubular cylinder.

The *NeuRobot* system (Fig. 2.6) is a equipped by an endoscope containing irrigant and channels that allows to insert scissors, forceps, micro-needle and laser tip for the manipulation of tissues [17]. Surgeons command the slave manipulator by using three levers on the operating console and a 3D monitor. The robot is able to move the neuroendoscope towards the target following a precise trajectory and avoiding critical regions. Patient anatomy has to be previously derived using 3D MRI data sets of the brain. Surgeons gestures are physically constrained by high force wall provided by the robot [17].

The HUMAN system is a master slave microsurgery system suitable for MR-

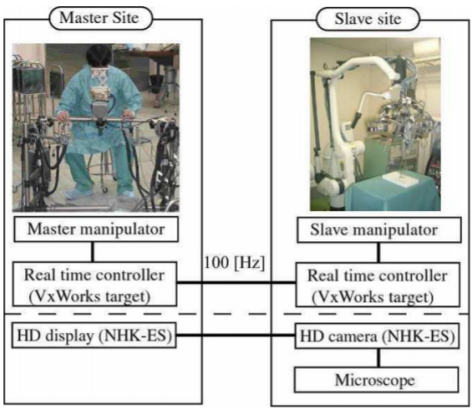

Figure 2.8: Advanced micro-neurosurgical robotic system for the deep surgical field: Master workstation (left) and slave manipulator (right) equipped with a 3D microscope.

guided neurosurgery interventions. The manipulator is MR-compatible and includes an endoscope, a perfusion tube, a suction tube and two micro-forceps with two DOF. The MR-guided system is able to perform accurate positioning of the end-effector with respect to the target as well as guiding it to execute safe moves [43].

A high-powered surgical microscope is integrated in the solution proposed by Baba et al. [7] which is expected to be used for operations in the deep surgical field. The system consists of three parts: a 3-dimensional microscope system, the master manipulators which are the interface devices and the slave manipulators that actually perform surgical gestures (Fig. 2.8). The slave is composed by two arms holding the surgical tools. Each arm has three DOF and one translational DOF in the insertion axis. The microscope must provide a good depth perception and in the developed system a high definition surgical view is presented on the 3D display system at the master site. However, performing accurate and dexterous movements in micromanipulation technique is very challenging in submillimiter workspaces.

Numerous robotic systems have been developed to assist surgeons in avoiding

Figure 2.9: The Craniostar, an active robotic wheeled tool for surgical craniotomy, is shown.

sensitive structures, such as vessels, in microneurosurgical interventions; however, they have not seen widespread clinical use due to drawbacks such as large size, obtrusiveness in the cramped surgical field, inability to adapt to changing conditions, limited function, inadequate integration with existing clinical workflow, increased operative time and high cost. All these drawbacks can be alleviated implementing avoidance zones and automatic force control within a completely handheld active instrument. Thus, surgeon's training, dexterous manipulation capability and ability to adapt are retained. Handheld tools bring safety advantages since they have limited and the surgeon can quickly react if unexpected events occur.

The only handheld tool developed for neurosurgery application is the Craniostar which is an active robotic wheeled tool for surgical craniotomy [31] (Fig. 2.9). The robot is integrated in a SNS that employs a tracking system and a graphic user interface for the visualization of preoperative images, mostly from the CT. The advantages of semi–automatic approach with respect to teleoperation-based methods have been widely explained in the recent literature [51, 18, 35].

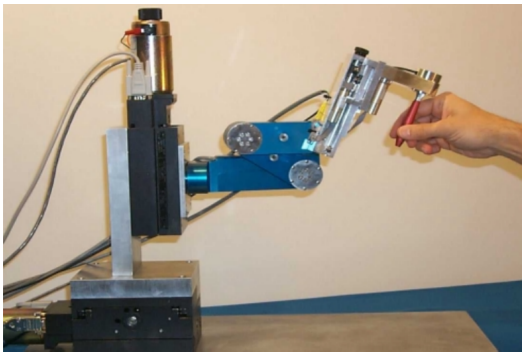

Figure 2.10: The Steady Hand manipulator is a collaborative robot developed for intraocular laser surgery. It is able to detect the force applied by the operator, suppress physiological tremor and compensate for unintended movements.

2.3 Collaborative and handheld robots for microsurgery

Microsurgery operations are very delicate procedures that usually deal with structures with cross sections from millimiters to microns [14]. Therefore, accuracy and dexterity in micromanipulation can be affected by physiological tremor, drifts, *wander* (slow trends) and *jerk* (sporadic fast jumps) [38]. In order to improve the quality of surgeons performance, suppressing involuntary movements that may affect surgical outcomes, collaborative and handheld robots have been introduced.

Taylor et al. [65] developed the *Steady Hand* (Fig. 2.10) for intraocular surgery that is a cooperative system actively coupled with a controlled robot arm. The robot's controller is equipped with force sensors that detect the force exerted by the operator to the tool and the strain applied by the tool to the tissue. Force/torque information is used as input to the controller which is able to perform smoothing and tremor compensation. It is capable to suppress tremor and involuntary hand movements in the order of 50-100 μm. The main advantages of the *Steady Hand* system with respect to master-slave technology are the reduced cost, user acceptance and the ease of use since they kept tool's size and weight as similar

Figure 2.11: First prototype of Micron.

as possible to passive instruments. However, handheld robotic instruments are also extremely suitable for microsurgery because they can face safety and liability issues, preserving surgeon tactile feedback.

2.3.1 Early Micron prototypes

The first handheld tool prototype for microsurgery was introduced by Cameron Riviere's research group in the "Surgical Mechatronics Laboratory" (Robotics Institute, Carnegie Mellon University, Pittsburgh, PA, USA) in 2003 [53].

The instrument, called Micron (Fig. 2.11), is an handheld tool equipped with piezoelectric actuators able to compensate for tremor by the actuation of the end-point to counteract the involuntary hand motion. The first prototype featured seven piezoeletric stacks in series that provided 3 DOF to the micromanipulator. Thus, the motors between the handle-grip and the end-effector allowed the tip to move semi-independently regardless to the hand motion. Moreover, the Micron is able to sense its own motion and to exploit advance filtering techniques in order to separate desired and undesired motions thanks to a 6 DOF inertial sensing module.

Later, a new design of the handheld micromanipulator was proposed in order to overcome the drawbacks of the first prototype, such as the high cost and the weight. For the second prototype they used a mechanical amplification on the actuation [6]. However, they figured out that inertial sensors were not suitable to precisely detect motion at frequencies below 10 Hz. Hence, a new Micron

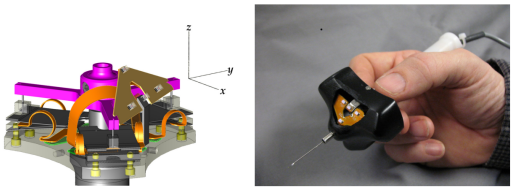

Figure 2.12: 3-DOF Micron prototype with piezo-biomorph actuators (left) and a set of 3 LED (right).

set-up was proposed that featured an optical tracking system, the Apparatus to Sense Accuracy of Position (ASAP) [16]. For the 3-DOF Micron (Fig. 2.12) the range of motion was increased replacing the piezoeletric stacks with piezo-biomorph actuators on a large base [38]. The need of increasing the DOF and range of motion for pratical applications lead to development of the last version of the handheld tool, the 6-DOF Micron [72], largely described in Sec. 3.5.1. The specifications of the five different Micron prototypes are summerized in Table 2.1.

Table 2.1: Micron Overview.

Prototype	DOF	Actuator	Sensor	Range of Motion (mm)	Dimension (mm)	Weight(g)	Features
Micron [53]	3	Piezoelectric	IMU	$0.56 \times 0.56 \times 0.1$	$\varnothing$ 22 $\times$ 180	170	Piezoelectric stacks without mechanical amplification
Micron [6]	3	Piezoelectric	IMU	$0.56 \times 0.56 \times 0.1$	$\varnothing$ 20 $\times$ 180	100	Mechanical amplification
Micron [16]	3	Piezoelectric	Optical tracking	$0.35 \times 0.43 \times 0.08$	$\varnothing$ 22 $\times$ 58.5	-	Flexure-based
3-DOF Micron [38]	3	Piezo-biomorph	Optical tracking	$2.0 \times 2.0 \times 0.4$	$\varnothing$ 50 $\times$ 120	-	Semi-automated operation
6-DOF Micron [72]	6	Piezolinear	Optical tracking	$\varnothing$ 4.0 $\times$ 4.0	$\varnothing$ 28.5 $\times$ 126	70.0	Fully-automated operation

Control aids

The robotic control aids the Micron provides are classified as tremor compensation, virtual fixtures and motion scaling [13].

Tremor compensation Tremor compensation aims at suppressing high-frequency involuntary hand movements with amplitude over 100 μm [58]. Combining filters between the hand motion and the drive mechanism it is possible to eliminate specific frequency bands and to accomplish user's intended gestures.

Virtual Fixtures Virtual Fixtures (VF) are spatial motion constraints generated with computer vision techniques that provide supports to surgeon while performing manipulation tasks. In surgical applications, VF generated from the anatomy have been integrated into robotic systems in order to limit movements in specific zones with the aim of enhancing safety [24]. VF may be exploited not only to guide the end–effector to reach a target but also to define forbidden regions that need to be avoided in order to improve surgical outcomes. They limit manipulator's movements into restricted regions and/or drive its actions along desired paths (hard VF). VF implementations will be described in detail in Sec. 3.4.

Motion scaling Instead of implementing hard VF that do not allow any deviations from the constraint they impose, it can be useful to introduce soft VF that leave the operator free to override them. It is possible to set the entity of the constraint they provide defining a motion scaling factor. Motion scaling reduces movements so that the tip can move a fraction of the hand movement and allows to share control between the surgeon and the VF. It is often combined with tremor compensation. Recently, as described by Tabares et al [64], a low-pass shelving filter, able to carry out either motion scaling or tremor suppression, has been

developed for Micron. It has proved to reduce involuntary hand movements of 30-50% more with respect to low-pass filters.

Chapter 3

Materials and Methods

The algorithm proposed in the present work can be divided in four parts, as shown in Fig. 3.1:

1. Segmentation algorithm (Sec. 3.1);
2. Inter-frame tracking (Sec. 3.2);
3. 3D reconstruction (Sec. 3.3);
4. Virtual fixtures (Sec. 3.4).

The segmentation algorithm allows segmenting the vessel(s) of interest (i.e. the vessel(s) to avoid) in microscopy images with a deformable-model approach. Vessels are then tracked in time with Kalman filtering and motion estimation given by Optical Flow (OF). 3D vessel reconstruction is used to find the vessel spatial coordinates in the Micron control reference system (i.e. to define the 3D coordinates of the region to avoid). The VF implement the vessel collision avoidance task, preventing the manipulator to enter into the defined avoidance zone.

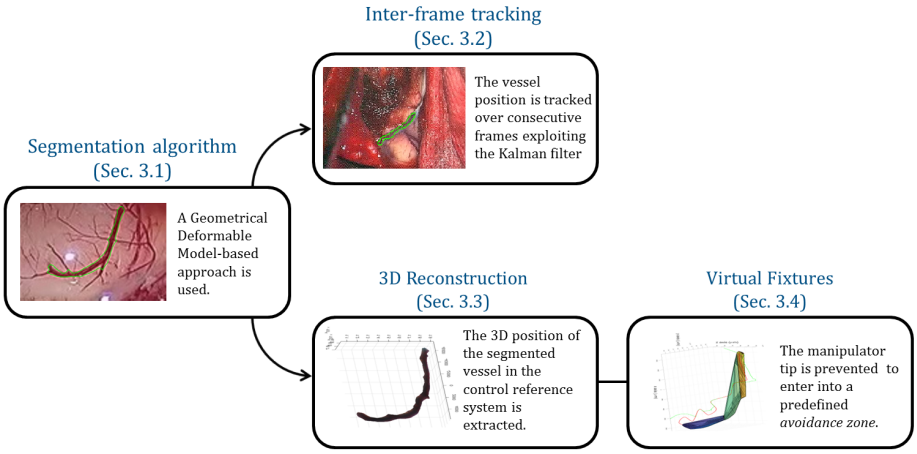

Figure 3.1: Workflow of the proposed algorithm for vessel avoidance in neurosurgery.

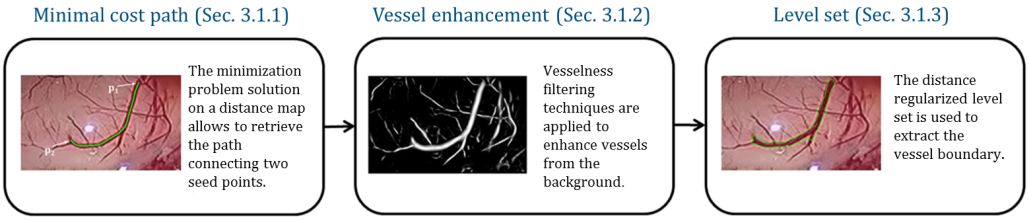

Figure 3.2: Workflow of the vessel segmentation algorithm.

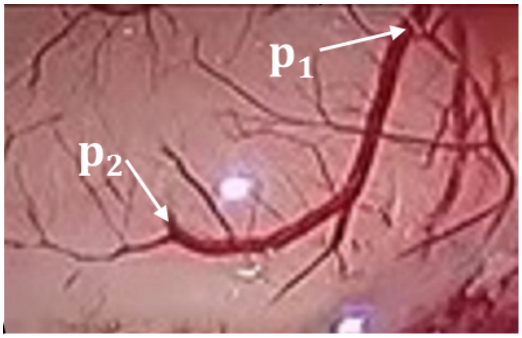

Figure 3.3: Manual selection of the starting point $\mathbf{p_1}$ and the ending point $\mathbf{p_2}$ of the vessel of interest in a microscope video frame.

3.1 Segmentation algorithm

In this work, a Geometrical Deformable Model (GDM)–based approach, that requires only the manual selection of two seed points ($\mathbf{p1}$ and $\mathbf{p2}$), is used to segment vessels in microscopy frames (Fig. 3.3). The $\mathbf{p1}$ and $\mathbf{p2}$ are connected employing the Minimal Cost Path (MCP) algorithm (Sec. 3.1.1). The obtained path is used as initialization of the GDM algorithm, which acts on an enhanced version of the image, obtained as described in Sec. 3.1.2. The GDM is formulated as a Level-Set (LS) algorithm (Sec. 3.1.3). The workflow of the proposed algorithm is shown in Fig. 3.2.

3.1.1 Minimal Cost Path

The MCP algorithm requires to define a cost function inside the image domain Ω. Such cost fuction is minimized to retrieve the minimum cost path ($C_{\mathbf{p_1},\mathbf{p_2}}$) between $\mathbf{p_1}$ and $\mathbf{p_2}$. The cost function here used is the Minimal Action Map ($U : \Omega \longrightarrow \mathbb{R}^+$), shown in Fig. 3.4. U is computed as the minimum of the energy's integral along the path between $\mathbf{p_1}$ and all the image points $\mathbf{x} \in \Omega$:

$$\forall \mathbf{x} \in \Omega, U(\mathbf{x}) = \min_{\gamma \in \mathbf{A}_{p_1,\mathbf{x}}} \int P(\gamma(s), \gamma'(s))ds \tag{3.1}$$

where $\mathbf{A}_{p_1,\mathbf{x}}$ represents the set of paths connecting each $\mathbf{x}$ to $\mathbf{p_1}$, which, it is worth noting, corresponds to the only minimum of U.

P is the potential measure relative to an infinitesimal distance along the path γ. P is defined in accord to the anisotropic tensor metric M (symmetric definitive positive) as follow:

$$P(\gamma(.), \gamma'(.)) = \sqrt{\gamma'(.)^T M(\gamma(.))\gamma'(.)} \tag{3.2}$$

with:

$$M(\gamma(.)) = v * \Lambda * v^T \tag{3.3}$$

being $v = [\mathbf{v_1}; \mathbf{v_2}]$, with $\mathbf{v_1}$ and $\mathbf{v_2}$ image Hessian (H(x,y)) eigenvectors and $\Lambda = [\lambda_1 \quad 0; 0 \quad \lambda_2]$, with λ_1, λ_2 image H eigenvalues.

$H(x, y)$ for an image ($I(x, y)$) is defined as:

$$H(x,y) = \begin{bmatrix} \frac{\partial^2 I(x,y)}{\partial x^2} & \frac{\partial^2 I(x,y)}{\partial x \partial y} \\ \\ \frac{\partial^2 I(x,y)}{\partial y \partial x} & \frac{\partial^2 I(x,y)}{\partial y^2} \end{bmatrix} \tag{3.4}$$

Image partial derivatives are obtained convolving I with the partial derivatives of a Gaussian kernel with standard deviation σ. Multi-scale analysis is performed using different σ values.

To obtain U, Eq. 3.1 is solved with recursive Fast Marching Method (FMM) [32]. Gradient descent (Runge–Kutta method) is then used to find the minimal path $C_{\mathbf{p_1},\mathbf{p_2}}$ from $\mathbf{p_2}$ to $\mathbf{p_1}$.

$$\frac{dC_{\mathbf{p_1},\mathbf{p_2}}}{ds}(s) \propto -M^{-1}(C_{\mathbf{p_1},\mathbf{p_2}}(s))\nabla U(C_{\mathbf{p_1},\mathbf{p_2}}(s)) \tag{3.5}$$

with $C_{\mathbf{p_1},\mathbf{p_2}}(0) = \mathbf{p_2}$.

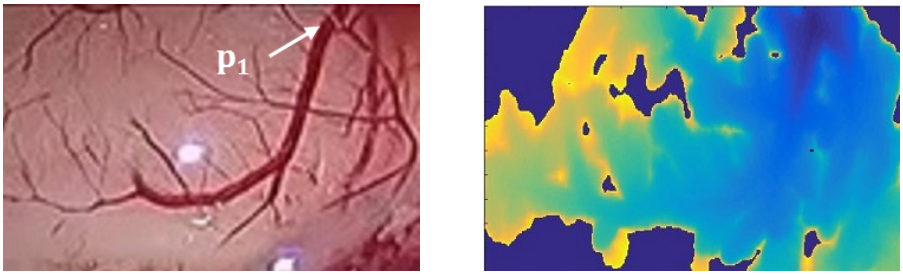

(a) **(b)**

Figure 3.4: Original image (a) and corresponding Minimal Action Map (b). The user-defined starting point $\mathbf{p_1}$ represents the unique minimum in the Map.

3.1.2 Vessel enhancement

Vesselness enhancement is used as a preprocessing step for vessel segmentation with GDM. Specifically, the filter proposed by Frangi et al. [21] is here used:

$$\nu_0 = \begin{cases} 0 & if \lambda_2 > 0, \\ \exp(-\frac{R_B^2}{2\beta^2})(1-\exp(-\frac{S^2}{2c^2})) \end{cases}$$

being R_B a measure of deviation from blob-like structure:

$$R_B = \frac{\lambda_1}{\lambda_2} \tag{3.6}$$

S, the Frobenius matrix norm of H:

$$S = \parallel H \parallel_F = \sqrt{\sum_{j<2} \lambda_j^2} \tag{3.7}$$

and β and c constants. A multi-scale implementation is performed, to take into account vessels of different size. A visual example of vessel enhancement is shown in Fig. 3.5.

3.1.3 Level Set

The LS method is used to obtain the vessel segmentation from the minimal path $C_{\mathbf{p_1},\mathbf{p_2}}$, obtained as described in Sec. 3.1.1. In the LS formulation, $C_{\mathbf{p_1},\mathbf{p_2}}$, which

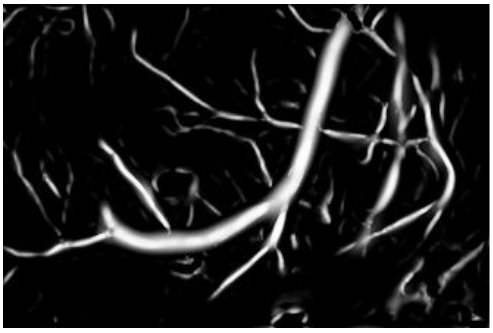

Figure 3.5: Vessel enhancement obtained through the vesselness measure for the geometric deformable model evolution. The vesselness represents the likelihood that a pixel belongs to a blood vessel.

Figure 3.6: Distance regularized region-based level set used to implement the evolution of the deforming curve.

for simplicity we refer to as C, is implicitly represented as the zero level set of a time-dependent scalar function f. Formally, C is defined as $C = \{x : \Omega(x,t) = 0\}$. The LS guides the C evolution according to:

$$\frac{\partial \phi}{\partial t} = -f(x,y)|\nabla \phi| \tag{3.8}$$

The f can be formulated according to image intensity, gradient or higher image derived terms [8]. In this case, the enhanced image obtained in Sec. 3.1.2 is used. For the LS problem solution, the momentum based optimization theory is used [34]. A visual example of the segmentation result is shown in Fig. 3.6.

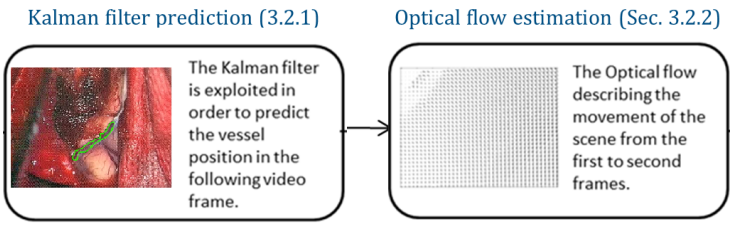

Figure 3.7: The inter-frame tracking algorithm consists of two steps: Kalman filter prediction and Optical flow estimation.

3.2 Inter-frame tracking

The vessel tracking between consecutive microscopy frames exploits Kalman filtering prediction. From the segmented vessel contour in the t^{th} video frame (p_t), the Kalman prediction ($\hat{p}_{t+1}$) of the vessel contour position in the $(t+1)^{th}$ frame provides the initialization for the actual contour (p_{t+1}) segmentation. The vessel segmentation is then achieved with GDM. The tracking method is summarized in Fig. 3.7.

3.2.1 Kalman filter prediction

The Kalman filter estimate is defined as:

$$\hat{p}_{t+1} = A_t \, p_t \quad p_t = \begin{bmatrix} x \\ y \end{bmatrix} \tag{3.9}$$

being A the Kalman transition matrix:

$$A = \begin{bmatrix} \frac{x_t+u}{x_t} & 0 \\ 0 & \frac{y_t+v}{y_t} \end{bmatrix} \tag{3.10}$$

Visual example of Kalman filter estimate are shown in Fig 3.8.

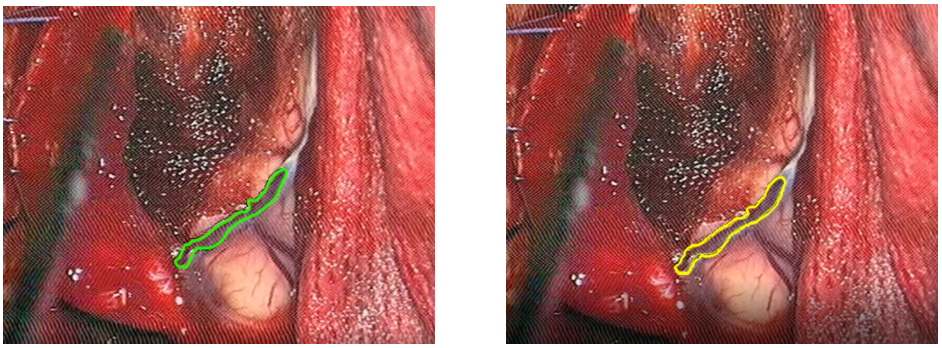

(a) **(b)**

Figure 3.8: Vessel tracking in an image sequence over time: (a) Segmentation in the t^{th} frame. (b) Tracking in the $(t+1)^{th}$ frame.

3.2.2 Optical flow estimation

The Kalman transition matrix A is obtained by estimating the displacement between consecutive frames through the OF [60]. According to the original formulation of Horn and Schunck (HS) [30] OF models the distribution of motion velocities of brightness patterns in an image. [26]. The OF cannot be determined at a point in the image independently of surrounding points without introducing further constraints. The velocity field at each image point has two components whereas the image brightness changes at a point in the image plane introduces only one constraint. If brightness varies as a function of only one image coordinate, pattern motion in one direction yields brightness change at a particular point, but movements in the other direction does not cause any effects.

HS formulated the OF relying on brightness constancy and spatial smoothness theories. The method includes a data term, which considers some image properties constant, and a spatial term modeling the expected variation of the flow across the image. The algorithm works on the optimization of an objective function that embodies these two terms.

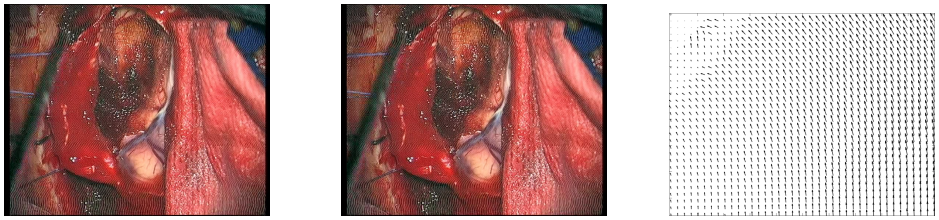

(a) **(b)** **(c)**

Figure 3.9: Optical flow computed between 2 subsequent video frames (a) frame acquired at time t (b) frame acquired at time t+1 (c) Vector field describing the movement between 2 subsequent video frames

The "classical" spatially discrete OF objective function is defined as follow:

$$\begin{aligned} E(\mathbf{u},\mathbf{v}) = \sum_{i,j} \{ & \rho_D(I_1(i,j) - I_2(i+u_{i,j}, j+v_{i,j})) \\ & + \lambda[\rho_S(u_{i,j} - u_{i+1,j}) + \rho_S(u_{i,j} - u_{i,j+1}) \\ & + \rho_S(v_{i,j} - v_{i+1,j} + \rho_S(v_{i,j} - v_{i,j+1})]\} \end{aligned} \tag{3.11}$$

u represents the horizontal component and v represents the vertical component of the OF field (discrete image displacements) which can be derived from the first image I_1 and the following one I_2. λ is called regularization parameter and ρ_D and ρ_S are the data and spatial penalty functions. The algorithm relies on the Rudin-Osher-Fatemi structure texture decomposition method in order to increase the robustness against light changes [54]. A multi-resolution approach is employed in order to optimize the flow estimation. Given d, the downsampling factor, the standard deviation of the Gaussian anti-aliasing filter applied is equal to $\frac{1}{\sqrt{2d}}$.

Basically the algorithm uses the OF estimation at the raw level to warp the second frame on the first one at a higher level. This step allows to extract the flow increment quantifying the mismatch between the first frame and the warped version of the second one. The flow increment is determined at each level after 10 warping steps. An example of OF between two subsequent video frames is shown

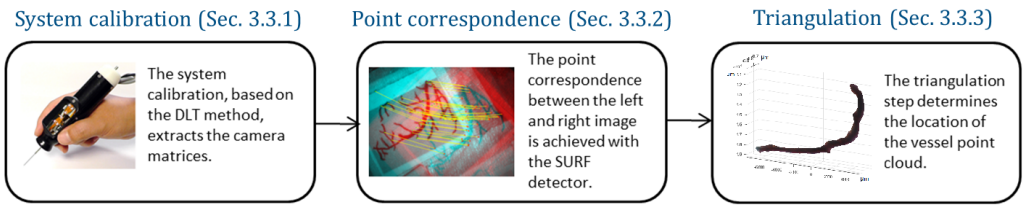

Figure 3.10: The 3D reconstruction method requires to perform the system calibration, to find the point correspondence and to apply the triangulation method.

in Fig. 3.9.

3.3 3D Reconstruction

The 3D reconstruction is performed in order to extract the 3D position of the segmented vessels in the Micron control reference system, i.e. the optical tracker reference system. The 3D recontruction operation requires a system calibration phase (Sec. 3.3.1) to find the camera calibration matrices. The point correspondence (Sec. 3.3.2) between two images of one scene acquired from the two cameras of the stereomicroscope are found. Once the matching point pairs and the camera matrices are determined, the 3D reconstruction is achieved with triangulation (Sec. 3.3.3). The 3D reconstruction workflow is shown in Fig. 3.10.

3.3.1 System calibration

Since the controller of the Micron works in the optical tracker reference system while the target is detected by the stereo-cameras, calibration mappings are mandatory. Essentially, calibration implies the registration of the 2D camera coordinates to the tracking system coordinate that actually are the Micron control 3D coordinates. The camera calibration requires to match a set of 3D tip positions measured by the optical tracker with a set of 2D locations detected from both left

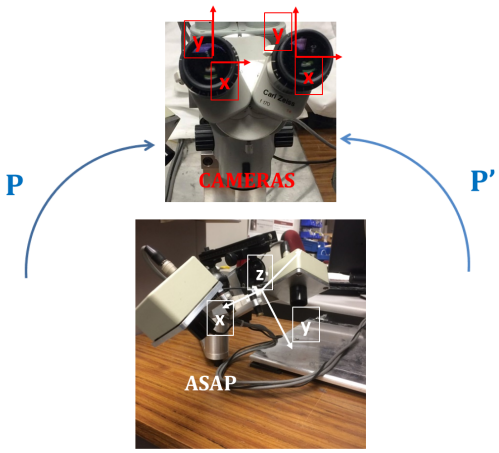

Figure 3.11: The camera matrices P and P' found during the calibration phase map a 3D point coordinates XYZ in the optical tracker reference system into the 2D coordinates of the cameras reference system XY.

and right cameras as described in detail in Appendix A. The camera matrices P and P' mapping a 3D point in the 2D camera reference system are reported in Fig. 3.11.

3.3.2 Point correspondence

A point pair consists of two points captured by the left and the right cameras that depict the same point in the real world. One of the main issue when dealing with displacement of a point from one image to another is that it is hard to find the exact pixel-to-pixel correspondence. The pixel value can change because of the light and the noise so finding the matching can be trivial. In the present work, the Speeded Up Robust Features (SURF) algorithm [42] is used in order to derive the transformation from the left to the right camera views by extracting the same key point in both images. It is a scale and rotation-invariant interest point detector that can basically be divided in three steps: detection, description and matching.

The feature detector method must be robust in order extract the key features

of an object independently on its position and orientation in the scene [12]. Thus, the interest points referring to the same object are extracted irregardless of the viewpoint.

The descriptors are features vectors that give a singular representation of the interest points.

The matching step allows to identify the correspondence among the interest points based on the similarity measure of their feature vectors. The geometric transform that maps the key points in the left image to the key points in the right image is estimated. Hence, the corresponding point pairs among the two images are derived.

SURF detector algorithm

Detection The SURF detector is based on the determinant of H in order to detect corner points at the intersection of two edges [42]. A key point is detected when in its neighborhood the algorithm finds strong derivatives along two dominant and different edge directions. The hessian operator is based on the H derived from the expansion of the Taylor series in the neighborhood of the corner point. The local change around the point X is represented by the determinant of H and interest points are chosen among those whose determinant is maximal:

$$det(H(x)) = \frac{\partial^2 I}{\partial x^2}\frac{\partial^2 I}{\partial y^2} - \left(\frac{\partial^2 I}{\partial x \partial y}\right)^2 \tag{3.12}$$

Image partial derivatives are obtained convolving the image with the partial derivatives of a Gaussian kernel with standard deviation σ. Different values of σ are used to for multi-scale analysis. The key points are identified in the left image (Fig. 3.12a) and the right image (Fig. 3.12b).

Description The *descriptors* refer to a specific property of the neighborhood surrounding every interest point, such as the distribution of intensity. These fea-

(a) (b) (c)

Figure 3.12: The SURF detector algorithm extracts the image interest points characterized by unique feature vectors. (a) Feature points detected in the left image. (b) Feature points detected in the right image. (c) A matching point pair is found when the distance between their feature vectors is the smallest among all.

ture vectors have to be peculiar but also have to disclose robustness against noise, photometric variations, deformations and detection errors. They are retrieved with the Haar- wavelet transform.

Matching Finally, the algorithm works matching the *descriptors* between different images considering the distance between vectors. In order to increase the matching speed the algorithm considers the sign of the trace of H, the Laplacian:

$$\nabla^2 L = tr(H) = \frac{\partial^2 I}{\partial x^2} + \frac{\partial^2 I}{\partial y^2} \tag{3.13}$$

The sign of the Laplacian allows to discriminate between bright objects on a dark background and dark objects on a bright background. It speeds up the matching procedure because two descriptor vectors are compared only if their Laplacians have the same sign. An example of point matching is shown in Fig. 3.12c.

Geometric transform estimation

Once the matching step has been performed, the projective geometric transform is retrieved in order to map one image on the other one by using the M-estimator SAmple Consensus algorithm [66]. It allows to estimate the geometric transform

that links two images related to each other. It is a variant of the RANdom SAmple Consensus algorithm that is an iterative method that works on the estimation of the parameters of a mathematical model. The considered dataset contains "outliers", due to experimental errors so data that do not fit a model. The "inliers" are the real data of interest because their distribution can be interpreted assigning the right parameters to the model. Given a predefined distance threshold, a point of pairs p_i^l and p_i^r is considered inlier when the distance between p_i^r and the projection of p_i^l obtained applying the transformation is lower than the threshold. A projective transformation is a combination of several transformations (translation, rotation, isotropic scaling, nonisotropic scaling and tilting) and for the 2D-2D registration problem it is defined by nine parameters. It has 8 DOF so, in order to derive these parameters theoretically at least four point matching pairs are required. The projective transformation matrix, shown in 3.13 is defined as M_p:

$$M_p = \begin{bmatrix} a_{11} & a_{12} & a_{13} \\ a_{21} & a_{22} & a_{23} \\ a_{31} & a_{32} & a_{33} \end{bmatrix} \tag{3.14}$$

The distance is computed as:

$$D = \sqrt{(\hat{u} - \hat{w}x)^2 + (\hat{v} - \hat{w}y)^2} \tag{3.15}$$

where $[x\ y\ 1]$ is the point of interest and $[\hat{u}\ \hat{v}\ \hat{w}]$ its projection obtained applying M_p according to the following relation:

$$[\hat{u} \quad \hat{v} \quad \hat{w}] = [x \quad y \quad 1]M_p \tag{3.16}$$

The algorithm works iteratively relying on the computation and comparison of a distance metric. First, M_p is initialized as a matrix of zeros; at each iteration four pairs of corresponding points are chosen randomly and the nine parameters of M_p are estimated. If the updated M_p has a distance metric lower than the previous

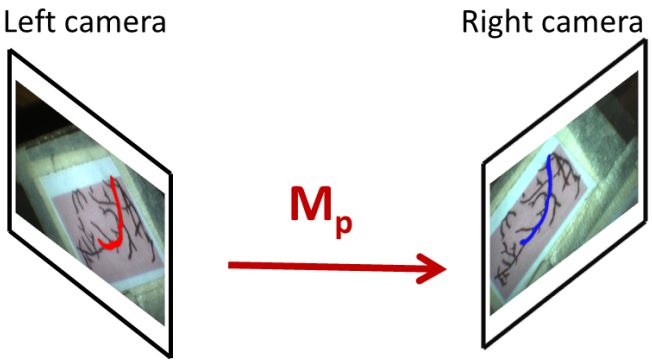

Figure 3.13: The projective matrix M_p represents the geometric transformation that maps a point in the left image to its corresponding point in the right image.

one, then the algorithm replaces it with the new estimate. The loop proceeds until the distance becomes less than a predefined threshold or the maximum number of iteration has been reached. Given the transformation matrix and the set of points defining the vessel in the left image , the corresponding points in the right image are found through a simple mapping operation (Fig. 3.13).

3.3.3 Triangulation

The triangulation operation and the metric 3D geometry allows to determine the location of the vessel points X_i in the 3D world in order to extract the vessel point cloud. The method is described in Appendix B. Applying the triangulation to every point pairs belonging the vessel, the point cloud in 3D is retrieved as depicted in Fig. 3.14.

3.4 Virtual Fixtures

The forbidden-region VF implements the vessel collision avoidance task, preventing the manipulator to enter into a predefined avoidance zone, representing the

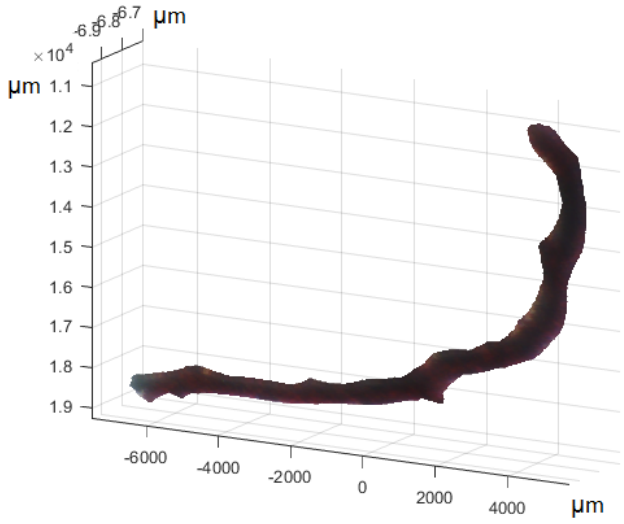

Figure 3.14: The point cloud defining the vessel spatial extent is retrieved applying the triangulation algorithm to every image point pairs.

segmented vessel and a cylindrical safety zone surrounding it. The control command is triggered as soon as the distance d between the tool tip and the vessel surface becomes lower than the cylindrical radius. Each time a new tip position sample is detected by the optical tracking system, the algorithm finds the closest point x_s belonging to the vessel surface and computes d. The Micron tip is driven to reach a point distant d_{safety} (i.e. the cylindrical radius) from x_s if d is less than d_{safety}.

3.4.1 Volume reconstruction

The VF algorithm requires to define the bounding surface of the point set in 3D in order to reconstruct the vessel volume. The method proposed by Barber et al [10], called Quickhull algorithm, is able to face this issue because it allows to model a geometrical shape on a point cloud in the 3D world. The convex hull implementation is explained in depth in Appendix C.

Vessels cannot be considered in general convex objects because of their cur-

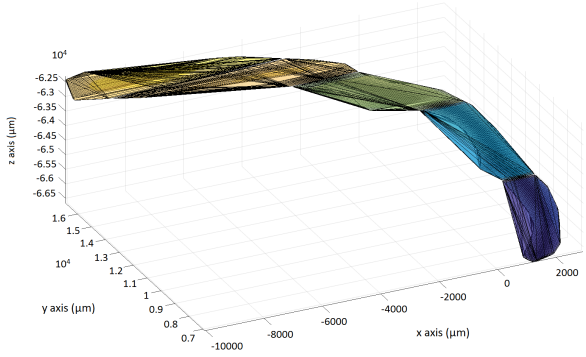

Figure 3.15: The volume defining the vessel of interest is reconstructed applying the convex hull to five subsets of the point cloud. The convex hull is a mesh of triangles that includes all the points belonging to the point set.

vature; there can be straight lines connecting two points of the set that do not lie exclusively inside the object. Building a convex hull that encompasses the whole retrieved point cloud could lead to erroneous results since the volume would not follow the original vessel shape. In order to overcome this limit several subsets are extracted from the original point cloud and for each subset a convex hull is built and linked to the adjacent ones. In Fig. 3.15 the point cloud is divided in five subsets.

3.4.2 Vessel avoidance algorithm

The implemented vessel avoidance algorithm belongs to the class of forbidden-region VF, since it prevents the manipulator from entering into reconstructed forbidden areas. Once the tracking system has detected the current tip position and the 3D point cloud has been retrieved, the shortest line connecting the query point and the triangulation in 3D is found. The algorithm finds the closest point belonging to the vessel surface (x_s) and commands the Micron tip to reach a point distant d_{safety} from that point. The initial tip position (x_{init}), the closest point on

Forbidden-region VF algorithm

for all $x_i \in$ POINT CLOUD

compute distance(x_i, x_{init})

find $\bar{d}$: min distance(x_i, x_{init}) and x_s : $\bar{d}$=$|x_s$-$x_{init}|$

end all

if $x_{init} \in$ CONVEX HULL

x_{fin}= x_{init} + (x_s-x_{init})*(d_{safety} + $\bar{d}$)/ $\bar{d}$

else

if $\bar{d}$ < d_{safety}

x_{fin}= x_s + d_{safety} *(x_{init}-x_s)/ $\bar{d}$

else

x_{fin}=x_{init}

end if

end if

Table 3.1: The forbidden-region VF algorithm checks if the distance of the current tip position x_{init} from the surface $\bar{d}$ is lower than the safety distance d_{safety}. If it happens the Micron tip is commanded to reach a point distant d_{safety} from the surface, x_{fin}.

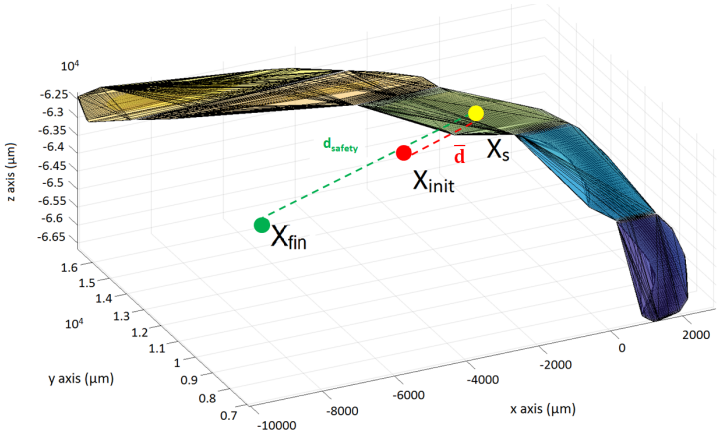

Figure 3.16: The algorithm checks if the distance $\bar{d}$ of the tip from the surface it is lower than d_{safety}. If so, the VF algorithm finds the projection of the tip position (x_{init}) on the vessel surface (x_s) and commands the Micron tip to reach a point distant d_{safety} from x_s (x_{fin}).

the surface (x_s) and the final tip position (x_{fin}) must be collinear points. The algorithm checks if the distance d of the tip from the surface it is lower than d_{safety}, as described in Table 3.1 and shown in Fig. 3.16.

3.5 System setup

The Micron setup includes: the Micron manipulator, an ASAP tracking system and a ZEISS stereo operating microscope (Fig.3.17).

3.5.1 Micromanipulator design

6-DOF Micron is a handheld micromanipulator that features a parallel-link mechanism (Fig. 3.19b), the Gough-Stewart platform [59], instead of a serial-link mechanism ($\varnothing \approx 25$ mm) like the previous prototypes. A piezoelectric linear motor, the SQUIGGLE® motor (SQL-RV-1.8, New Scale Technologies, Inc, USA) was used to realize the manipulator because of its small size (2.8 mm $\times$ 2.9 mm $\times$ 6 mm) and the adequate force it is able to generate (0.3 N at 3.3V). The prototype

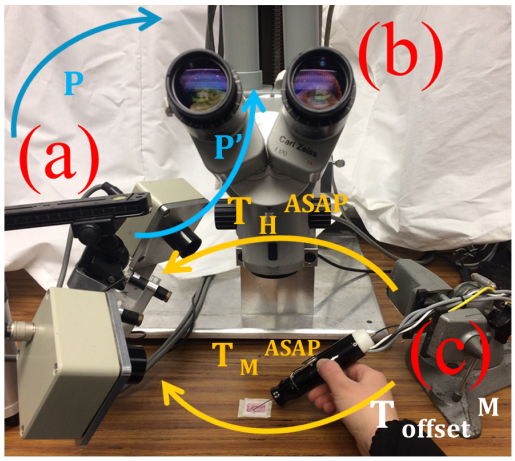

Figure 3.17: System setup: (a) ASAP tracking system; (b) Zeiss stereo operating microscope; (c) Micron manipulator. The ASAP detects two sets of LED, one on the moving platform and one on the handle. Triangulating the LED the system retrieves the position (t_H and t_M) and orientation (director cosines) of the reference systems of the handle (T_H^{ASAP}) and the moving platform (T_M^{ASAP}) with respect to the ASAP reference system. The camera matrices P and P' found during the calibration phase are used to map a 3D point coordinates in the ASAP reference system into the 2D coordinates of the cameras reference system.

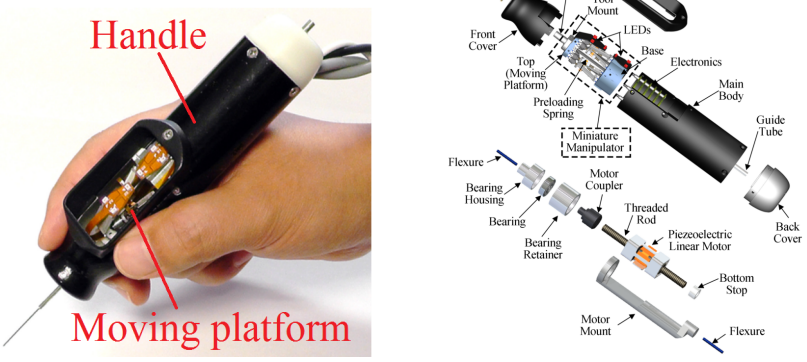

(a) **(b)**

Figure 3.18: 6-DOF Micron prototype. The handle and the moving platform are shown. (a) View of the prototype. (b) View of the handheld manipulator assembly (top) and the linear actuation module (bottom).

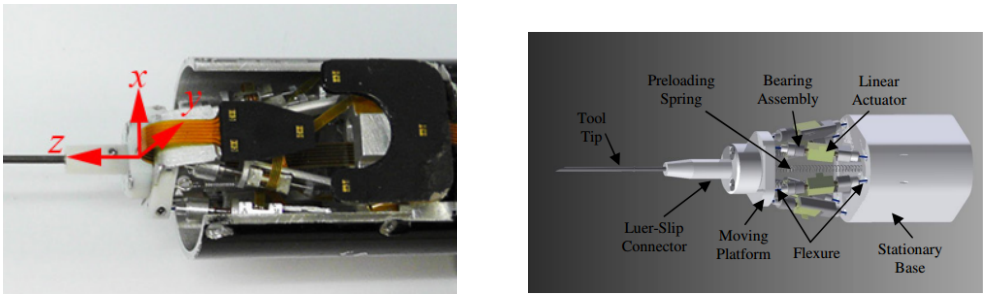

(a) **(b)**

Figure 3.19: (a) The 6-DOF Micron kinematics: 3 DOF for the translation along X, Y and Z at the instrument tip, 2 DOF for the translation in XY plane at a point along the shaft and 1 DOF for the axial rotation. (b) Parallel-link mechanism of Micron. The null position corresponds to the tip position when Micron is not controlled and the moving platform and the base are parallel. The Micron tip position corresponds to the end-effector coordinates when a command is sent to Micron.

and its components are shown in Fig. 3.18. A Proportional-Integral-Derivative (PID) controller commands the Micron that deals with the inverse kinematics defining the goal position and the current position of the tool tip in terms of six link-lenghts. Tremor and any other undesired movement are considered as disturbances to control. The Micron system architecture is described in detail in Fig. 3.20. The reachable workspace covers a cylindrical volume 4 mm long and 4 mm in diameter (Fig. 3.21).

Kinematics

In terms of kinematics the new prototype features 6 DOF (Fig. 3.19a):

- 3 DOF for the translation along X, Y and Z in the Euclidean space at the instrument tip;
- 2 DOF for the translation in XY plane at a point along the instrument shaft;
- 1 DOF for the axial rotation of the instrument.

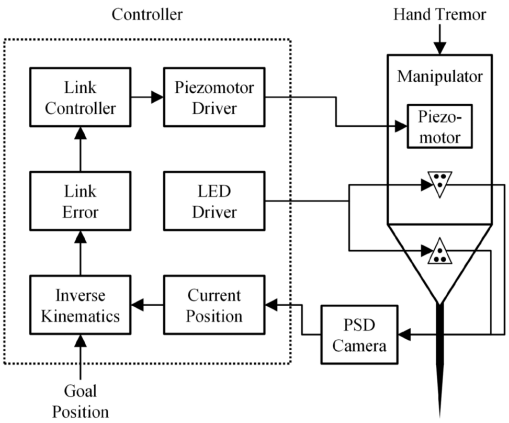

Figure 3.20: Micron system architecture.

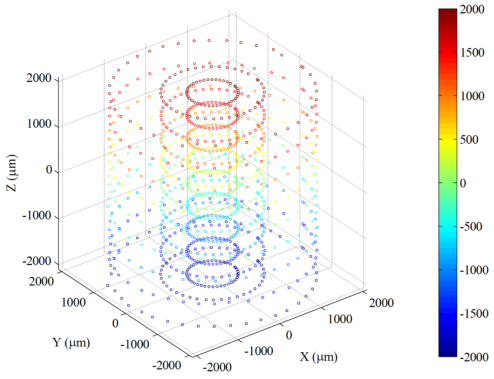

Figure 3.21: Points reached by the Micron in the workspace: a 4-mm diameter cylinder 4 mm tall.

3.6 ZEISS stereo operating microscope

The visual setup is composed by a stereo operating microscope (High-power Zeiss OPMI®1, Carl Zeiss, AG, Germany) that can reach magnifcations from 4X up to 25X equipped with two CCD (Charge-Coupled Device) cameras (Flea®2, Point Grey Research, Richmond, BC, Canada) able to acquire videos at 30 Hz and with a resolution of 800x600 pixels.

3.7 ASAP tracking system

In order to localize either the tip or the handle in the workspace the system setup includes an optical tracking system, the ASAP. Two sets of infrared LEDs are mounted to the Micron, three of these are placed in the moving platform and the other three on its handle. The Position Sensitive Detectors (PSD), or lateral-effect photodiodes, of the ASAP provide position information at a sampling rate of 1 kHz over 27 cm^3 workspace and with a reduced Root Mean Square (RMS) noise (10 μm) [72]. Frequency-domain-multiplexed PSDs enable to measure multidimensional position and orientation by simultaneously detecting the position of the centroid of multiple modulated sources [39].

The triangulation of the LEDs position in 3D allows to retrieve the pose of the handle and the tip.

3.7.1 Network interface

The Micron network interface is via two User Datagram Protocol (UDP) packets to reduce latency. Micron sends out status packets to the workstation via Ethernet at 1000 times a second (1 kHz update rate), holding the values of many internal signals. It is possible to send a command packet at whatever rate. The previous

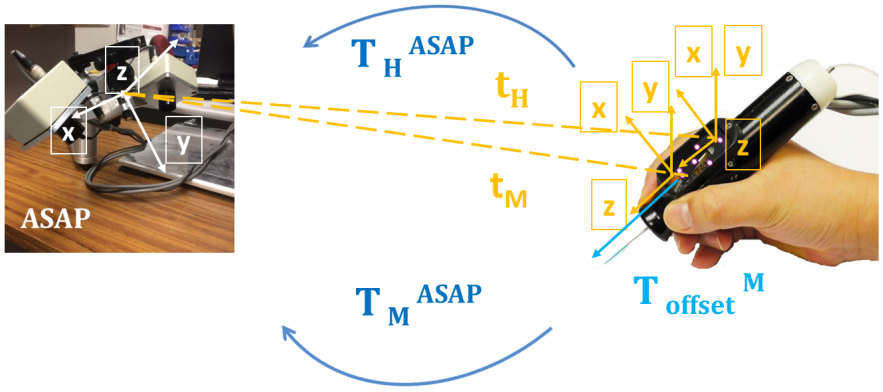

Figure 3.22: The ASAP detects two sets of LED, one on the moving platform and one on the handle. Triangulating the LEDs the system retrieves the position (t_H and t_M) and orientation (director cosines) of the reference systems of the handle (T_H^{ASAP}) and the moving platform (T_M^{ASAP}) with respect to the ASAP reference system.

command remains in effect until a new one is sent. The basic trace record is composed of triples of single precision floating point numbers. There are currently 60 triples. Each status packet has an additional triple at the beginning which is the same as the header of the data file. It has two additional 32 bit integers at the end, the trace index and the sequence number. So, the packet size is: 4 (bytes per float) * 3 (floats per triple) * 61 (triples, including header) + 4 (bytes per int) * 2 = 740 bytes. Among the 60 triples, the Micron status packet carries information about (Fig. 3.22):

- The 3D position of the six LEDs on the moving platform and on the handle;
- The three components of the translation vector t_M that identifies the origin of the moving platform reference system with respect to the ASAP reference system;
- The three components of the translation vector t_H that identifies the origin of the handle reference sytem with respect to the ASAP reference system;

- The director cosines describing the orientation of the x, y and z axis of the moving reference system with respect to ASAP reference system;
- The director cosines describing the orientation of the x, y and z axis of the handle reference system with respect to ASAP reference system;
- The null tip position that corresponds to the Micron tip position without control when the base and the moving platform are parallel;
- The current tip position that corresponds to the Micron tip position estimated triangulating the LEDs.

The 3D coordinates of the goal position is sent to Micron via UDP packets as well. Thus, the transformation matrix in homogeneous coordinates that allows to map a point from the moving platform reference system to the ASAP reference system is derived:

$$T_M^{ASAP} = \begin{bmatrix} cos\alpha_x & cos\alpha_y & cos\alpha_z & T_{Mx} \\ cos\beta_x & cos\beta_y & cos\beta_z & T_{My} \\ cos\gamma_x & cos\gamma_y & cos\gamma_z & T_{Mz} \\ 0 & 0 & 0 & 1 \end{bmatrix} \tag{3.17}$$

as well as T_H^{ASAP} that maps a point defined in the handle reference system to the ASAP reference system :

$$T_H^{ASAP} = \begin{bmatrix} cos\alpha'_x & cos\alpha'_y & cos\alpha'_z & T_{Hx} \\ cos\beta'_x & cos\beta'_y & cos\beta'_z & T_{Hy} \\ cos\gamma'_x & cos\gamma'_y & cos\gamma'_z & T_{Hz} \\ 0 & 0 & 0 & 1 \end{bmatrix} \tag{3.18}$$

Given, the T_{offset} in the moving platform reference system found during the calibration phase (Appendix A):

$$T_{offset}^M \begin{bmatrix} 0 & 0 & l_0 & 1 \end{bmatrix}^T \tag{3.19}$$

the actual tip position with respect to the ASAP reference frame P_{tip}^{ASAP} is estimated as follow:

$$P_{tip}^{ASAP} = T_{M}^{ASAP} T_{offset}^{M} \tag{3.20}$$

If Micron is not controlled the null tip position corresponds to the Micron tip position sensed by the ASAP since the moving platform and the base are parallel to each other. When a command is sent, since the orientation of the moving platform with respect to the base is known, it is possible to retrieve the null tip position dealing with the tip position detected by the ASAP. The optical tracking system, the ASAP, run in parallel with the controller of the Micron because they are integrated in the same LABVIEW® machine. It is possible to extract ASAP positioning information, accomplish stereo visual servoing and give control commands to the Micron in real-time [14].

3.8 Material

As to evaluate the segmentation algorithm (Sec. 3.1) and the inter-frame tracking (Sec. 3.2), microscopy videos recorded from real CM e MVD interventions were used. Video acquisition characteristics are reported in Sec. 3.8.1. To assess the reliability of the 3D reconstruction (Sec. 3.3) and the VF (Sec. 3.4), phantom images were employed. Phantoms are obtained as described in Sec. 3.8.2. A summary of the material used for the evaluation is reported in Fig. 3.23. The algorithms described in the previous sections of this chapter were all implemented in Matlab®.

3.8.1 Intra-operative image acquisition

The material for the present work was collected recording two microscopy videos during the standard surgical routine at Istituto Neurologico C. Besta in Milan,

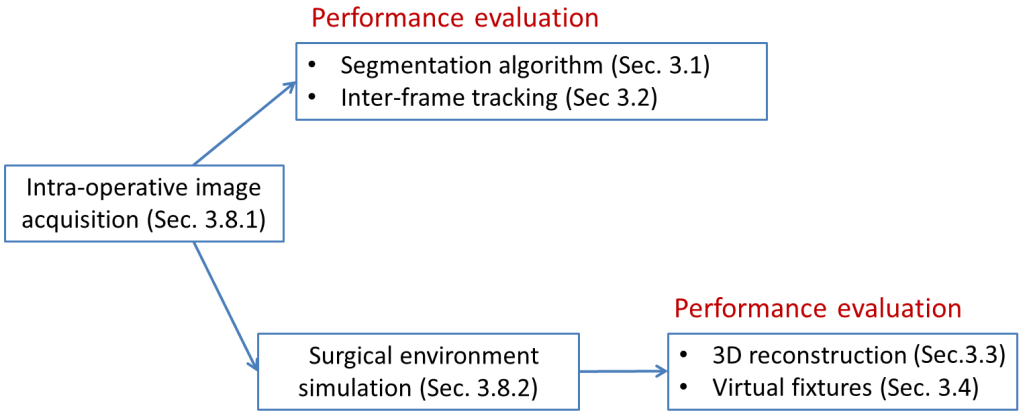

Figure 3.23: Material used for evaluating the proposed approach.

Italy. The videos refer to a MVD intervention (Fig. 3.24a) that lasted about four hours and a CM resection (Fig. 3.24b) that lasted two hours. Both operations were performed using the Zeiss OPMI Pentero® 900 surgical microscope (ZEISS, Oberkochen, Germany) (Fig. 3.25) with a 3.5-5X magnification. The microscope technical specifications are described in detail in Table 3.2. The vessel segmentation algorithm was tested on fifty microscopy video frames acquired during two neurosurgery interventions at Istituto Neurologico Carlo Besta (Milan, Italy). The tracking algorithm was evaluated on two video clips during one minute of acquisition.

3.8.2 Surgical environment simulation

In order to simulate the surgical environment two flat patterns (Fig. 3.26) that reproduce the vessels to avoid were printed (≈20x15 mm) and captured by the left camera and the right camera of the Micron stereomicroscope (800x600 pixels). The 3D reconstruction algorithm was tested on twenty images (ten of each pattern) acquired by the left and the right camera of the stereomicroscope (4X

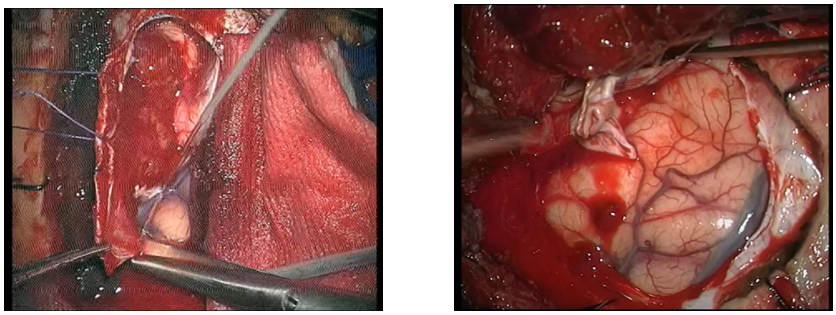

(a) **(b)**

Figure 3.24: Video frames acquired from the surgical microscope used at Istituto Neurologico Carlo Besta: (a) microvascular decompression and (b) convexity meningioma resection.

Figure 3.25: Zeiss OPMI Pentero ® 900 surgical microscope used during the standard surgical routine at Istituto Neurologico C. Besta (Milan, Italy)

Technical data	
Rated voltage	(115 V): 100 V-125 V
	(230 V): 220 V-240 V
Rated frequency	50 Hz-60 Hz
Weight	365 kg
Apochromatic optics	Motorized focus: Varioskop®
	with working distance 200-500 mm
	Motorized zoom; 1:6 zoom ratio
	10x magnetic widefield eyepieces with integrated eyecups
	Autofocus with 2 visible laser dots,
	automatic mode with magnetic brakes
Illumination	Superlux® 330 light source
	with 2 x 300 W xenon
	Automatic Iris Control for adjusting the illumination
	to the field of view
	Individual light threshold setting
Video	Integrated 3-CMOS HD video camera
	22”HD video touchscreen
	Integrated video still image capturing on HDD and USB-media
Connectivity	Navigation interface
	Interface for micromanipulator
	Remote diagnosis via internet/VPN
	DICOM module for patient data transfer

Table 3.2: Technical specifications of the Zeiss OPMI Pentero® 900 microscope.

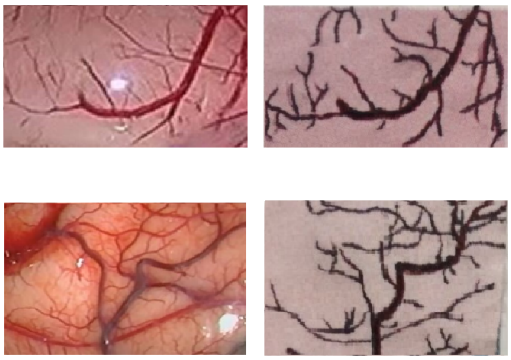

Figure 3.26: Orginal video frames (left) and corresponding printed patterns (right).

magnification). For the VF performance evaluation, a flat pattern was used to let Micron interact with phantom vessels. The vessel avoidance algorithm was tested in real time by operating Micron above an image of the vascular pattern and making repeated attempts to cross the blood vessel while in contact with the surface. The trial lasted 400 s and the chosen d_{safety} was 1.6 mm.

3.9 Evaluation methods

3.9.1 Segmentation algorithm

The reliability of the automatic segmentation was evaluated and quantified in terms of Accuracy (Acc), Sensitivity (Se), Specificity (Sp) and Dice Similarity Coefficient (DSC). The performance indexes were computed comparing the results obtained with the automatic segmentation to the results of the manual segmentation, elected as GS (Fig. 3.27a). Basically, two binary images were studied where the value 1 indicates the vessel points and the value 0 refers to the background points. The class of interest includes the points belonging the manually-segmented vascular structure representing the ground truth region. It is the set of point covering the white part in Fig. 3.27b.

In order to define Acc, Se, Sp and DSC it is useful to introduce four categories of points:

- The True Positive (TP) points are the pixels that the algorithm correctly classifies as belonging to the class of interest;
- The True Negative (TN) points are the pixels that the algorithm correctly classifies as not belonging to the class of interest;
- The False Positive (FP) points are the pixels incorrectly classified as belonging to the class of interest;
- The False Negative (FN) points are the pixels incorrectly classified as not belonging to the class of interest.

The confusion matrix is a 2x2 matrix that shows the relationships between prediction and measurement results and tabulates these four categories, as shown in Table 3.3.

	GS condition positive	GS condition negative
condition positive	TP	FP
condition negative	FN	TN

Table 3.3: Confusion matrix

Given N= TP+TN+FP+FN, A the binary image obtained with the automated method, B the binary image obtained with the manual method and P the number of occurrences, the performance indexes are derived as follow:

- Acc = (TP+TN)/N;
- Se = TP/(TP+FN);

(a) **(b)**

Figure 3.27: Definition of the ground truth. (a) Manual segmentation of the vessel of interest. (b) Binary image extracted from the manual segmentation of the vessel of interest.

- Sp = TN/(TN+FP);
- DSC= 2*P[(A=1)∩(B=1)]/ [P(A=1)+P(B=1)]

They all provide a statistical evaluation of the automatic segmentation performance but in different ways. Acc reveals the ability of the algorithm to discriminate the set of pixels belonging to the vessel surface and the one belonging to the background. Se describes the likelihood of the algorithm to classify correctly the vessel points. It is given by the ratio between the number of pixels found as vessel points and the actual number of vessel pixels defined by the ground truth. Sp indicates the likelihood of the algorithm to classify correctly the background points. It is determined computing the ratio between the number of pixels found as belonging to the background and the actual number of background pixels specified by the ground truth. DSC quantifies how similar the automated algorithm and the manual segmentation results are. It is found as the number of overlapped pixels belonging to the vessels divided by the sum of the vessel points in the two images.

3.9.2 Inter-frame tracking

The performance indexes Acc, Se, Sp and DSC, defined in Sec. 3.9.1, were computed to evaluate the performance of the inter-frame tracking algorithm. The segmentation obtained through the Kalman prediction followed by the LS method was compared to the GS-manual segmentation applied in consecutive video frames.

3.9.3 3D reconstruction

Reprojection error

The accuracy of the 3D reconstruction is strongly related to the quality of the system calibration as well as the quality of the point matching. The 3D coordinates of a point are derived using the camera's internal and external parameters and the 2D coordinates of the corresponding point pairs, as described in Appendix B. In the ideal case of epipolar geometry the projections of the 3D point into the image planes are obtained tracing a line that passes through their focal points. Since any kind of errors in the parameters estimation and in the point matching affects the 3D reconstruction, the projection lines may not have any point in common and the 3D point is found with the mid-point method. In order to quantify how accurately a 3D point estimate reproduces the real point in 3D, all the points of the point cloud are projected back into the left and the right images. The 2D coordinates of the reprojected points are found as PX_i and $P'X_i$, given P and P' the projection camera matrices. Being u' and u'_i the detected matching point pairs used for the triangulation, the *reprojection errors* r_{left} and r_{right} are defined as the Euclidean distance in pixel between each detected point and its reprojected point (Fig. 3.28) in the left and right cameras respectively:

$$r_{left} = d(u_i, PX_i) \quad and \quad r_{right} = d(u'_i, P'X_i) \tag{3.21}$$

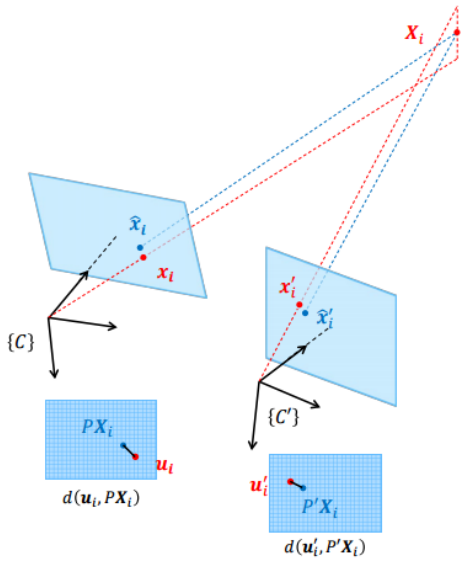

Figure 3.28: The 3D reconstruction accuracy is measured computing the point reprojection errors. The reprojection error d(u_i, PX_i) represents the distance in pixel between the 2D point x_i and its corresponding world point X_i projected back into the same image $\hat{x}_i$. *C* and *C'* are the focal points of the left and the right cameras.

Spatial error

Since the reprojection error is a relative measure because it is expressed in pixel and the pixel size can vary depending on the distance between the microscope and the patterns, the spatial error was also considered. The spatial error S_{err} is an absolute measure that allows to quantify the 3D reconstruction accuracy in mm. In order to compute the spatial error and assess the quality of the proposed method it is useful to use an object whose dimensions can be physically measured. The vessels depicted on the patterns have not a regular shape and defining control points in order to find the distance between them can be tricky. Thus, the distances between the corners of the rectangular printed patterns were measured using a digital caliper with resolution 0.01 mm (Fig. 3.29). The printed patterns were acquired by both cameras and the same corner points, selected manually in the camera image, were triangulated in order to extract their locations in the ASAP

Figure 3.29: The digital caliper with a resolution of 0.01 mm used to measure the size of the rectangular printed patterns.

reference system. Their relative distances were then computed in mm. The spatial error S_{err} (Eq. 4.4) is based on the known spatial values of the pattern dimensions (the distance between two corners measured with the caliper d_m) compared to the computed values from the final 3D reconstruction (the distance between two triangulated corner points d_{3D}).

$$S_{err} = |d_m - d_{3D}| \tag{3.22}$$

Lens distortion was considered negligible.

3.9.4 Virtual Fixtures

The distance of the Micron tip from the vessel surface over time was found for three cases:

- With the VF on and the goal position sent to Micron by the VF controller (desired trajectory);
- With VF on and the tip position sensed by the ASAP (trajectory with control);
- If the VF were off (trajectory without control).

These measures are found as the Euclidean distance between the Micron tip and the its projection on the vessel surface. The Wilcoxon signed-rank test (significance level $\alpha = 0.05$) was used for paired sample to assess whether the desired trajectory significantly differs from the one obtained with and without control.

In order to assess the performance of Micron, an error measure was computed as the Euclidean distance in mm between the goal position P_G sent to the manipulator by the VF controller and the tip position P_T sensed by the ASAP tracking system:

$$\epsilon_d = d(P_T, P_G) \tag{3.23}$$

The number of times that the Micron tip is distant from the surface less than d_{safety} (n) over the total (N) is computed as described in the following equation:

$$\sigma_d = \frac{n}{N} \times 100 \tag{3.24}$$

Three cases are considered: when the VF are off, when the VF are on and the goal position is sent to Micron and when the VF are on and the Micron tip position is sensed by the ASAP.

Chapter 4

Results

4.1 Automatic segmentation algorithm

The distribution of Acc, Se, Sp and DSC describing the performance of the automatic segmentation (Fig. 4.1a) with respect to the manual segmentation (Fig. 4.1b) is shown in Fig. 4.2a. The related values of 1^{st} quartile, median, 3^{rd} quartile and Inter-Quartile Range (IQR) are reported in Table 4.1.

(a) **(b)**

Figure 4.1: (a) Automatic segmentation of the vessel of interest. (b) Manual segmentation of the vessel of interest, elected as GS.

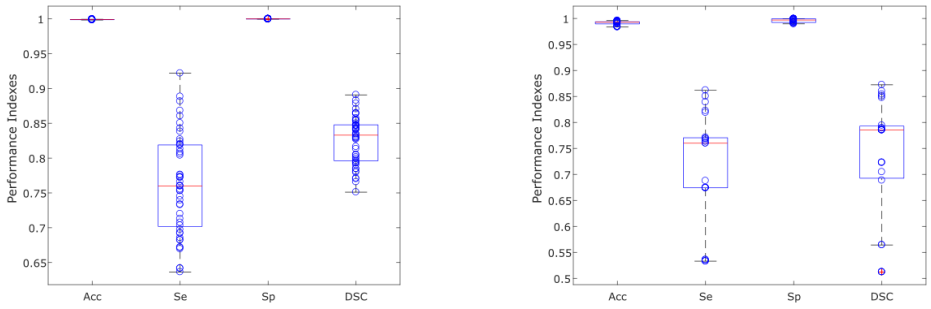

(a) **(b)**

Figure 4.2: Accuracy (Acc), sensitivity (Se), specificity (Sp) and Dice similarity coefficient (DSC) of the automatic segmentation algorithm compared with the manual segmentation (a) and of the inter-frame tracking algorithm compared with the manual segmentation (b).

	q_1	$\tilde{x}$	q_3	IQR
Acc	0.9987	0.9990	0.9991	4.0e-04
Se	0.7004	0.7600	0.8189	0.1185
Sp	0.9997	0.9998	0.9999	2.0e-04
DSC	0.7956	0.8329	0.8485	0.0529

Table 4.1: Automatic segmentation algorithm performance. Acc= Accuracy; Se = Sensitivity; Sp= Specificity; DSC=Dice similarity coefficient; q_1= 1^{st} quartile; $\tilde{x}$=median; q_3= 3^{rd} quartile; IQR=Inter-Quartile Range.

4.2 Inter-frame tracking

The performance of the tracking algorithm are described through boxplot representation in terms of Acc, Se, Sp and DSC (Fig. 4.2b). Table 4.2 summarizes the distribution values of the considered performance indexes.

	q_1	$\tilde{x}$	q_3	IQR
Acc	0.9870	0.9927	0.9937	0.0067
Se	0.6742	0.7600	0.7951	0.1209
Sp	0.9919	0.9970	0.9993	0.0074
DSC	0.6264	0.7854	0.8491	0.2227

Table 4.2: Tracking algorithm performance. Acc= Accuracy; Se= Sensitivity; Sp= Specificity; DSC= Dice similarity coefficient; q_1= 1^{st} quartile; $\tilde{x}$=median; q_3= 3^{rd} quartile; IQR=Inter-Quartile Range.

4.3 3D reconstruction

4.3.1 Reprojection error

The reprojection errors statistics are presented in Table 4.3.

	q_1	$\tilde{x}$	q_2	IQR
r_{left} [pixels]	0.6791	0.8890	1.4158	0.7367
r_{right} [pixels]	0.6901	0.8992	1.4276	0.7375

Table 4.3: Reprojection error [pixels] distribution. q_1= 1^{st} quartile; $\tilde{x}$=median; q_3= 3^{rd} quartile;; IQR=Inter-Quartile Range.

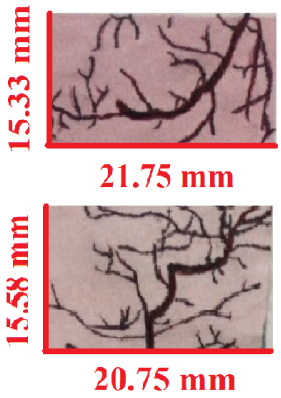

Figure 4.3: The size of the printed patterns measured with the digital caliper.

	q_1	x̃	q_2	IQR
S_{err} [mm]	0.1380	0.2960	0.4050	0.2670

Table 4.4: Statistics of the spatial error S_{err} $[mm]$ distribution. q_1= 1st quartile; x̃=median; q_3= 3rd quartile; IQR=Interquartile Range.

Spatial error

The statistics related to the spatial error S_{err} are reported in Table 4.4. The size of the printed pattern measured with the digital caliper are shown in Fig. 4.3.

4.4 Vessel avoidance algorithm

Using the real time VF algorithm, the Micron tip was forced to lift over the vessel (green trajectory in Fig. 4.4a) when the null position of the manipulator (red trajectory in Fig. 4.4a) was within a safety distance of 1.6 mm. The Micron tip trajectory sensed by the ASAP was recorded as well (blue in Fig. 4.4b). The Wilcoxon rank sum test revealed that there were statistically significant differences between the the desired trajectory and the trajectory without control (p-value$<\alpha$). The same test revealed that the desired trajectory and the trajectory with control are

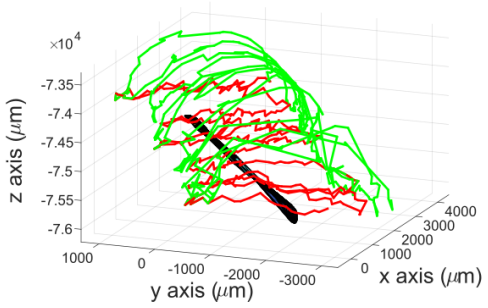

(a)

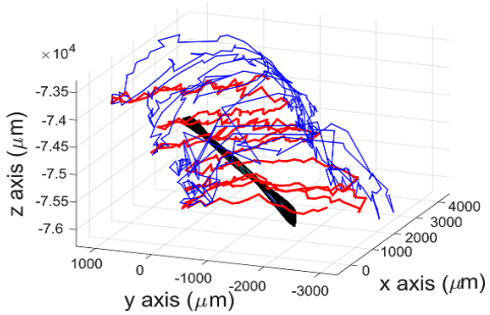

(b)

Figure 4.4: Real time application of the vessel avoidance algorithm. (a) The red trajectory refers to the Micron null positions (if the VF were off) whereas the green trajectory is given by the goal positions sent to Micron by the VF controller. (b) The red trajectory represents the Micron null positions while the blue trajectory refers to the tip positions detected by the ASAP with the VF enabled.

not statistically different since the p-value found was higher than α.

The distance measure *d* over time when the Micron controller is active (green), disabled (red) and the distance of the Micron tip from the surface according to the ASAP measurements (blue) is plotted in Fig. 4.5. The percentage values σ_d related to the same trial are shown in 4.5 whereas the statistics of the distance error ϵ_d are reported in Table 4.6.

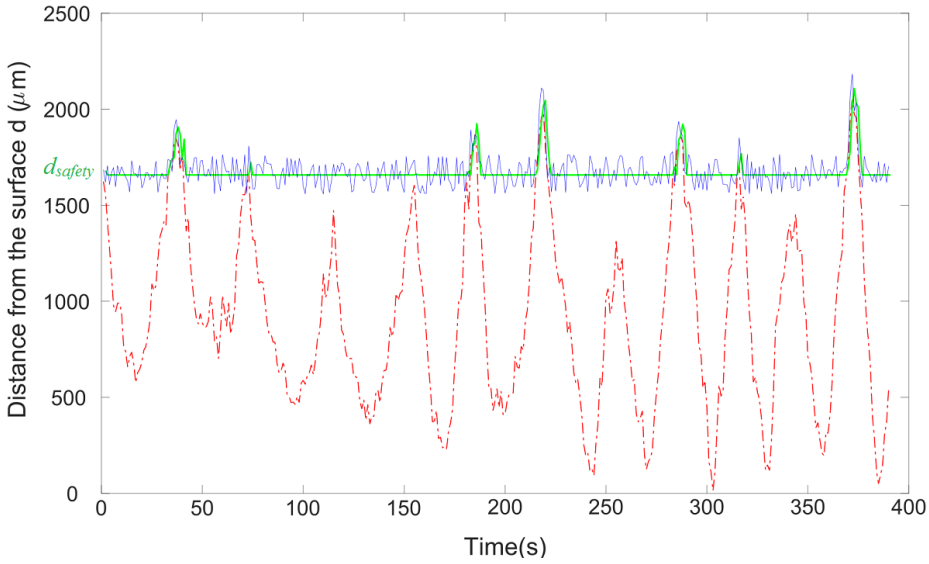

Figure 4.5: Distance d of the Micron tip from the vessel surface over time in three cases: i) if the VF were disabled (red), ii) with the VF enabled and the Micron goal tip positions sent by the VF controller (green) and iii) with the VF enabled and the Micron tip positions sensed by the ASAP (blue). The chosen safety distance d_{safety} is equal to 1.6 mm (1600 μm).

	VF OFF	VF ON (GOAL)	VF ON (ASAP)
σ_d	90.25 %	0 %	43.25%

Table 4.5: The percentage values σ_d reported refers to the ratio of tip position samples distant from the vessel surface less than d_{safety} to the total number of tip samples acquired in 400 s. Three cases are considered: i) if the VF were disabled, ii) with the VF enabled and the Micron goal tip position sent by the VF controller and iii) with the VF enabled and the Micron tip positions sensed by the ASAP.

	q_1	$\tilde{x}$	q_2	IQR
ϵ_d [mm]	0.0693	0.1037	0.1521	0.0827

Table 4.6: Statistics of the distance error ϵ_d $[mm]$ measured as the Euclidean distance between the tip position sensed by the ASAP tracking system and the goal position sent to Micron. q_1= 1st quartile; $\tilde{x}$=median; q_3= 3rd quartile; IQR=Interquartile Range.

Chapter 5

Discussion

Medical robots for neurosurgery have been a topic of research for over 20 years for their high precision, repeatability and endurance, but almost all such systems are teleoperated. Unlike any of the master-slave systems, the use of a handheld instrument offers considerable advantages in terms of easy to use, liability, safety and economy since it preserves the intuitive feel facilitating surgeons acceptance. The user, indeed, can remain in gross control of the tool motion during the whole intervention, able to adapt to changing conditions or to finish a procedure unaided in case of system failure. The proposed work provides a new approach to vessel avoidance for safe robotic assisted neurosurgery exploiting a handheld tool to reliably constrain surgeons' movements into predefined forbidden zones.

The performance of the segmentation algorithm applied to microscopy video frames was evaluated quantitatively with respect to the manual segmentation. The good results obtained in terms of Acc, Se, Sp and DSC highlight the reliability of the segmentation algorithm. The values of Acc and Sp are high whereas the values of Se and DSC are lower. Indeed, the manual segmentation, taken as GS, can have some limits. It can be hard to detect precisely the extremities and the boundaries of the structure of interest by hand. Moreover, since the number of

background pixels is much bigger than the number of pixels belonging to the vessel, the Se, that measures the proportion of positives, is largely affected by wrong vessel pixels classifications.

The tracking algorithm proved to successfully follow the vessel boundary motion since it gave comparable outcomes with respect to the manual segmentation applied singularly on consecutive video frames. Even though the values of Acc, Se, Sp and DSC are similar to the ones obtained for the automatic segmentation, they are slightly worse because some measures can be affected by wrong previous state estimates. However, the Kalman filter demonstrated to be an useful automatic tool to initialize the segmentation in consecutive video frames. If on the one hand the tracking algorithm is able to precisely follow the movement of the scene on the other hand its applicability is limited to the off-line case.

Both the segmentation and the tracking algorithm proved to efficiently overcome issues such as variations of brightness, different levels of illumination, image noise and intensity drops.

As for the reprojection errors analysis, the 3D reconstruction algorithm showed to accurately estimate the true vessel position since the values (in pixels) found were low for both left cameras and right cameras. The spatial error values attested the validity of the 3D reconstruction algorithm. However, the evaluation method for the spatial errors proposed in this thesis might disclose some limitations due either to the measuring device used or to the manual selection of corner points on the images.

The statistical analysis of the VF proved the effectiveness of the vessel avoidance algorithm. Indeed, the Wilcoxon rank sum test disclosed that there were statistically significant differences between the desired trajectory of Micron and the trajectory that would have been if the control were not triggered. Instead, the comparison between the desired trajectory and the trajectory with control, sensed

by the ASAP, showed that they do not differ significantly. Thus, even though the actual tip positions might be slightly far from the goal position, the contact of the tip with the vessel surface is prevented. Indeed, the results in terms of distance error proved the reliability of the real time VF algorithm, since the values found are largely lower than the safety distance.

Future works will aim at implementing a tracking algorithm for real time applications in order to take into account also tissue deformation and the presence of surgical tools in the scene, which can eventually occlude the vessel to be avoided. Thus, it can be effective to include an OF-failure recognition strategy. A 3D phantom that reproduces a more truthful surgical scenario will be further developed for testing.

Chapter 6

Table of acronyms

Acc Accuracy

ASAP Apparatus to Sense Accuracy of Position

CISS Constructive Interference in Steady State

CM Convexity Meningioma

CSF CerebroSpinal Fluid

CT Computer Tomography

DLT Direct Linear Transformation

DOF Degrees of Freedom

DSC Dice Similarity Coefficient

FMM Fast Marching Method

FN False Negative

FP False Positive

GDM Geometrical Deformable Model

GS Gold Standard

H Hessian

HS Horn Schunck

IQR Inter-Quartile Range

LS Level Set

MAM Minimal Action Map

MCP Minimal Cost Path

MF Matched Filtering

MPI Maximum Intensity Projection

MRI Magnetic Resonance Imaging

MVD MicroVascular Decompression

OF Optical Flow

PDE Partial Derivative Equation

PID Proportional-Integral-Derivative

PSD Positive Sensitive Detectors

RK4 Runge Kutta 4th order

Se Sensitivity

SNS Surgical Navigation System

Sp Specificity

SSD Sum of Square Distance

SURF Speeded Up Robust Features

TN True Negative

TP True Positive

UDP User Datagram Protocol

VF Virtual Fixtures

Bibliography

[1] [Online]. Available: http://www.mayfieldclinic.com/PE-rTGN.HTM.

[2] [Online]. http://www.sd-neurosurgeon.com/neurodiseases-meningiomas.php.

[3] [Online]. http://emedicine.medscape.com/article/341624-overview.

[4] [Online]. Available: http://www.abta.org.

[5] [Online]. Available: http://www.mountsinai.org/patient-care/service-areas/neurosurgery/areas-of-care/meningioma/types-of-meningiomas/convexity-meningioma.

[6] Wei Tech Ang, PK Pradeep, and CN Riviere. Active tremor compensation in microsurgery. In *Engineering in Medicine and Biology Society, 2004. IEMBS'04. 26th Annual International Conference of the IEEE*, volume 1, pages 2738–2741. IEEE, 2004.

[7] Shoichi Baba, Daisuke Asai, Shinichi Warisawa, Mamoru Mitsuishi, Akio Morita, Shigeo Sora, Ryo Mochizuki, and Takashi Shiraishi. Development of an advanced micro-neurosurgical robotic system for the deep surgical field. In *The First IEEE/RAS-EMBS International Conference on Biomedical Robotics and Biomechatronics, 2006. BioRob 2006.*, pages 437–442. IEEE, 2006.

[8] Souleymane Balla-Arabé, Xinbo Gao, and Bin Wang. Gpu accelerated edge-region based level set evolution constrained by 2d gray-scale histogram. *IEEE Transactions on Image Processing*, 22(7):2688–2698, 2013.

[9] Enzo Ballotta, Giuseppe Da Giau, Laura Renon, Surendra Narne, Marina Saladini, Elvira Abbruzzese, and Giorgio Meneghetti. Cranial and cervical nerve injuries after carotid endarterectomy: a prospective study. *Surgery*, 125(1):85–91, 1999.

[10] C Bradford Barber, David P Dobkin, and Hannu Huhdanpaa. The quickhull algorithm for convex hulls. *ACM Transactions on Mathematical Software (TOMS)*, 22(4):469–483, 1996.

[11] William A Barrett and Eric N Mortensen. Interactive live-wire boundary extraction. *Medical image analysis*, 1(4):331–341, 1997.

[12] Herbert Bay, Tinne Tuytelaars, and Luc Van Gool. Surf: Speeded up robust features. In *European conference on computer vision*, pages 404–417. Springer, 2006.

[13] Brian C Becker, Robert A MacLachlan, Gregory D Hager, and Cameron N Riviere. Handheld micromanipulation with vision-based virtual fixtures. In *Robotics and Automation (ICRA), 2011 IEEE International Conference on*, pages 4127–4132. IEEE, 2011.

[14] Brian C Becker, Sandrine Voros, Robert A MacLachlan, Gregory D Hager, and Cameron N Riviere. Active guidance of a handheld micromanipulator using visual servoing. In *Robotics and Automation, 2009. ICRA'09. IEEE International Conference on*, pages 339–344. IEEE, 2009.

[15] Subhasis Chaudhuri, Shankar Chatterjee, Norman Katz, Mark Nelson, and Michael Goldbaum. Detection of blood vessels in retinal images using two-dimensional matched filters. *IEEE Transactions on medical imaging*, 8(3):263–269, 1989.

[16] David Y Choi and Cameron N Riviere. Flexure-based manipulator for active handheld microsurgical instrument. In *Engineering in Medicine and Biology Society, 2005. IEEE-EMBS 2005. 27th Annual International Conference of the*, pages 2325–2328. IEEE, 2005.

[17] B Davies, Stephen Starkie, Simon J Harris, E Agterhuis, Volker Paul, and Ludwig M Auer. Neurobot: A special-purpose robot for neurosurgery. In *Robotics and Automation, 2000. Proceedings. ICRA'00. IEEE International Conference on*, volume 4, pages 4103–4108. IEEE, 2000.

[18] G Dogangil, BL Davies, and F Rodriguez y Baena. A review of medical robotics for minimally invasive soft tissue surgery. *Proceedings of the Institution of Mechanical Engineers, Part H: Journal of Engineering in Medicine*, 224(5):653–679, 2010.

[19] Parviz Dolati, Alexandra Golby, Daniel Eichberg, Mohamad Abolfotoh, Ian F Dunn, Srinivasan Mukundan, Mohamed M Hulou, and Ossama Al-Mefty. Pre-operative image-based segmentation of the cranial nerves and blood vessels in microvascular decompression: Can we prevent unnecessary explorations? *Clinical neurology and neurosurgery*, 139:159–165, 2015.

[20] Brian S Everitt. *Finite mixture distributions*. Wiley Online Library, 1981.

[21] Alejandro F Frangi, Wiro J Niessen, Koen L Vincken, and Max A Viergever. Multiscale vessel enhancement filtering. In *International Conference on Medical Image Computing and Computer-Assisted Intervention*, pages 130–137. Springer, 1998.

[22] M. M. Fraz, P. Remagnino, A. Hoppe, B. Uyyanonvara, A. R. Rudnicka, C. G. Owen, and S. A. Barman. Blood vessel segmentation methodologies in retinal images–a survey. *Computer methods and programs in biomedicine*, 108(1):407–433, 2012.

[23] William T Freeman and Edward H Adelson. The design and use of steerable filters. *IEEE Transactions on Pattern analysis and machine intelligence*, 13(9):891–906, 1991.

[24] Janez Funda, Russell H Taylor, Ben Eldridge, Stephen Gomory, and Kreg G Gruben. Constrained cartesian motion control for teleoperated surgical robots. *IEEE Transactions on Robotics and Automation*, 12(3):453–465, 1996.

[25] Mingcen Gao, Thanh-Tung Cao, Tiow-Seng Tan, and Zhiyong Huang. A 3d convex hull algorithm for graphics hardware. 2011.

[26] James J Gibson. On the analysis of change in the optic array. *Scandinavian Journal of Psychology*, 18(1):161–163, 1977.

[27] Junya Hanakita and Akinori Kondo. Serious complications of microvascular decompression operations for trigeminal neuralgia and hemifacial spasm. *Neurosurgery*, 22(2):348–352, 1988.

[28] Richard Hartley and Andrew Zisserman. *Multiple view geometry in computer vision*. Cambridge university press, 2003.

[29] TODA Hiroki, GOTO Masanori, et al. Patterns and variations in microvascular decompression for trigeminal neuralgia. *Neurologia medico-chirurgica*, 55(5):432, 2015.

[30] Berthold KP Horn and Brian G Schunck. Determining optical flow. *Artificial intelligence*, 17(1-3):185–203, 1981.

[31] Gavin Kane, Georg Eggers, Robert Boesecke, Jörg Raczkowsky, Heinz Wörn, Rüdiger Marmulla, and Joachim Mühling. System design of a hand-held mobile robot for craniotomy. In *International Conference on Medical Image Computing and Computer-Assisted Intervention*, pages 402–409. Springer, 2009.

[32] Ender Konukoglu, Maxime Sermesant, Olivier Clatz, Jean-Marc Peyrat, Hervé Delingette, and Nicholas Ayache. A recursive anisotropic fast marching approach to reaction diffusion equation: Application to tumor growth modeling. In *Information processing in medical imaging*, pages 687–699. Springer, 2007.

[33] G. Läthén, J. Jonasson, and M. Borga. Phase based level set segmentation of blood vessels. In *Pattern Recognition, 2008. ICPR 2008. 19th International Conference on*, pages 1–4. IEEE, 2008.

[34] Gunnar Läthén, Thord Andersson, Reiner Lenz, and Magnus Borga. Momentum based optimization methods for level set segmentation. In *International Conference on Scale Space and Variational Methods in Computer Vision*, pages 124–136. Springer, 2009.

[35] Win Tun Latt, Richard C Newton, Marco Visentini-Scarzanella, Christopher J Payne, David P Noonan, Jianzhong Shang, and Guang-Zhong Yang. A hand-held instrument to maintain steady tissue contact during probe-based confocal laser endomicroscopy. *IEEE transactions on biomedical engineering*, 58(9):2694–2703, 2011.

[36] Jesse D Lawrence, Andrew M Frederickson, Yue-Fang Chang, Patricia M Weiss, Peter C Gerszten, and Raymond F Sekula Jr. An investigation into quality of life improvement in patients undergoing microvascular decompression for hemifacial spasm. *Journal of Neurosurgery*, pages 1–9, 2017.

[37] David MacDonald, Noor Kabani, David Avis, and Alan C Evans. Automated 3-d extraction of inner and outer surfaces of cerebral cortex from mri. *NeuroImage*, 12(3):340–356, 2000.

[38] Robert A MacLachlan, Brian C Becker, Jaime Cuevas Tabarés, Gregg W Podnar, Louis A Lobes Jr, and Cameron N Riviere. Micron: an actively stabilized handheld tool for microsurgery. *IEEE Transactions on Robotics*, 28(1):195–212, 2012.

[39] Robert A MacLachlan and Cameron N Riviere. High-speed microscale optical tracking using digital frequency-domain multiplexing. *IEEE transactions on instrumentation and measurement*, 58(6):1991–2001, 2009.

[40] Ana Maria Mendonca and Aurelio Campilho. Segmentation of retinal blood vessels by combining the detection of centerlines and morphological reconstruction. *IEEE transactions on medical imaging*, 25(9):1200–1213, 2006.

[41] Suzanne M Michalak, John D Rolston, and Michael T Lawton. Incidence and predictors of complications and mortality in cerebrovascular surgery: National trends from 2007 to 2012. *Neurosurgery*, 2016.

[42] Krystian Mikolajczyk and Cordelia Schmid. Indexing based on scale invariant interest points. In *Computer Vision, 2001. ICCV 2001. Proceedings. Eighth IEEE International Conference on*, volume 1, pages 525–531. IEEE, 2001.

[43] Nobuhiko Miyata, Etsuko Kobayashi, Daeyoung Kim, Ken Masamune, Ichiro Sakuma, Naoki Yahagi, Takayuki Tsuji, Hiroshi Inada, Takeyoshi Dohi, Hiroshi Iseki, et al. Micro-grasping forceps manipulator for mr-guided neurosurgery. In *International Conference on Medical Image Computing and Computer-Assisted Intervention*, pages 107–113. Springer, 2002.

[44] Sara Moccia, Francesca Prudente, Elena De Momi, and Leonardo Mattos. Safety enhancement in robotic neurosurgery through vessel tracking. *6th Joint Workshop on New Technologies for Computer/Robot Assisted Surgery.*, 2016.

[45] Andrew P Morokoff, Jacob Zauberman, and Peter M Black. Surgery for convexity meningiomas. *Neurosurgery*, 63(3):427–434, 2008.

[46] Reza Nekovei and Ying Sun. Back-propagation network and its configuration for blood vessel detection in angiograms. *IEEE Transactions on Neural Networks*, 6(1):64–72, 1995.

[47] Mark Obermann. Treatment options in trigeminal neuralgia. *Therapeutic advances in neurological disorders*, 3(2):107–115, 2010.

[48] Dário AB Oliveira, Raul Q Feitosa, and Mauro M Correia. Segmentation of liver, its vessels and lesions from ct images for surgical planning. *Biomedical engineering online*, 10(1):1, 2011.

[49] S Bulent Omay and Gene H Barnett. Surgical navigation for meningioma surgery. *Journal of neuro-oncology*, 99(3):357–364, 2010.

[50] Shawna Pandya, Jason W Motkoski, Cesar Serrano-Almeida, Alexander D Greer, Isabelle Latour, and Garnette R Sutherland. Advancing neurosurgery with image-guided robotics: technical note. *Journal of neurosurgery*, 111(6):1141–1149, 2009.

[51] Christopher J Payne and Guang-Zhong Yang. Hand-held medical robots. *Annals of biomedical engineering*, 42(8):1594–1605, 2014.

[52] Kelvin Poon, Ghassan Hamarneh, and Rafeef Abugharbieh. Live-vessel: Extending livewire for simultaneous extraction of optimal medial and boundary paths in vascular images. In *International Conference on Medical Image Computing and Computer-Assisted Intervention*, pages 444–451. Springer, 2007.

[53] Cameron N Riviere, Wei Tech Ang, and Pradeep K Khosla. Toward active tremor canceling in handheld microsurgical instruments. *IEEE Transactions on Robotics and Automation*, 19(5):793–800, 2003.

[54] Leonid I Rudin, Stanley Osher, and Emad Fatemi. Nonlinear total variation based noise removal algorithms. *Physica D: Nonlinear Phenomena*, 60(1-4):259–268, 1992.

[55] Septimiu E Salcudean, S Ku, and G Bell. Performance measurement in scaled teleoperation for microsurgery. In *CVRMed-MRCAS'97*, pages 789–798. Springer, 1997.

[56] Nader Sanai, Michael E Sughrue, Gopal Shangari, Kenny Chung, Mitchel S Berger, and Michael W McDermott. Risk profile associated with convexity meningioma resection in the modern neurosurgical era: Clinical article. *Journal of neurosurgery*, 112(5):913–919, 2010.

[57] Raymond F Sekula, Andrew M Frederickson, Gregory D Arnone, Matthew R Quigley, and Mark Hallett. Microvascular decompression for hemifacial spasm in patients¿ 65 years of age: an analysis of outcomes and complications. *Muscle & nerve*, 48(5):770–776, 2013.

[58] SPN Singhy and CN Riviere. Physiological tremor amplitude during retinal microsurgery. In *Bioengineering Conference, 2002. Proceedings of the IEEE 28th Annual Northeast*, pages 171–172. IEEE, 2002.

[59] Doug Stewart. A platform with six degrees of freedom. *Proceedings of the institution of mechanical engineers*, 180(1):371–386, 1965.

[60] D. Sun, S. Roth, and M. J. Black. Secrets of optical flow estimation and their principles. In *Computer Vision and Pattern Recognition (CVPR), 2010 IEEE Conference on*, pages 2432–2439. IEEE, 2010.

[61] Garnette R Sutherland, Sanju Lama, Liu Shi Gan, Stefan Wolfsberger, and Kourosh Zareinia. Merging machines with microsurgery: clinical experience with neuroarm: Clinical article. *Journal of neurosurgery*, 118(3):521–529, 2013.

[62] Garnette R Sutherland, Isabelle Latour, Alexander D Greer, Tim Fielding, Georg Feil, and Perry Newhook. An image-guided magnetic resonance-compatible surgical robot. *Neurosurgery*, 62(2):286–293, 2008.

[63] Garnette R Sutherland, Paul B McBeth, and Deon F Louw. Neuroarm: an mr compatible robot for microsurgery. In *International congress series*, volume 1256, pages 504–508. Elsevier, 2003.

[64] Jaime Cuevas Tabarés, Robert A MacLachlan, Charles A Ettensohn, and Cameron N Riviere. Cell micromanipulation with an active handheld micromanipulator. In *2010 Annual International Conference of the IEEE Engineering in Medicine and Biology*, pages 4363–4366. IEEE, 2010.

[65] Russell Taylor, Pat Jensen, Louis Whitcomb, Aaron Barnes, Rajesh Kumar, Dan Stoianovici, Puneet Gupta, ZhengXian Wang, Eugene Dejuan, and Louis Kavoussi. A steady-hand robotic system for microsurgical augmentation. *The International Journal of Robotics Research*, 18(12):1201–1210, 1999.

[66] Philip HS Torr and Andrew Zisserman. Mlesac: A new robust estimator with application to estimating image geometry. *Computer Vision and Image Understanding*, 78(1):138–156, 2000.

[67] M Trope, Reuben R Shamir, Leo Joskowicz, Z Medress, G Rosenthal, A Mayer, N Levin, A Bick, and Yigal Shoshan. The role of automatic computer-aided surgical trajectory planning in improving the expected safety of stereotactic neurosurgery. *International journal of computer assisted radiology and surgery*, 10(7):1127–1140, 2015.

[68] Joseph Wiemels, Margaret Wrensch, and Elizabeth B Claus. Epidemiology and etiology of meningioma. *Journal of neuro-oncology*, 99(3):307–314, 2010.

[69] Asa J Wilbourn. Iatrogenic nerve injuries. *Neurologic clinics*, 16(1):55–82, 1998.

[70] Lei Xia, Jun Zhong, Jin Zhu, Yong-Nan Wang, Ning-Ning Dou, Ming-Xing Liu, Massimiliano Visocchi, and Shi-Ting Li. Effectiveness and safety of microvascular decompression surgery for treatment of trigeminal neuralgia: a systematic review. *Journal of Craniofacial Surgery*, 25(4):1413–1417, 2014.

[71] Feng Xu, Xing-ce Wang, Ming-quan Zhou, Zhongke Wu, and Xin-yu Liu. Segmentation algorithm of brain vessel image based on sem statistical mixture model. In *Fuzzy Systems and Knowledge Discovery (FSKD), 2010 Seventh International Conference on*, volume 4, pages 1830–1833. IEEE, 2010.

[72] Sungwook Yang. Handheld micromanipulator for robot-assisted microsurgery. 2015.

[73] Yong Yang, Shuying Huang, and Nini Rao. An automatic hybrid method for retinal blood vessel extraction. *International Journal of Applied Mathematics and Computer Science*, 18(3):399–407, 2008.

Appendix A

System calibration The camera matrix can be decomposed in five matrices that include the intrinsic and extrinsic parameters, as shown in Fig. A.1. The intrinsic parameters include focal length, principal point and lens distorsion while the extrinsic parameters are the position and orientation of the cameras. x_0 and y_0 define the offset of the principal point (the intersection of the line perpendicular to the image plane that passes through the camera center). f_x and f_y refer to the focal length, the distance between the camera center and the image plane, measured in pixels. s is the axis skew responsible for the shear distortion of the image. R and **t** are respectively the rotation matrix and the translation vector that describe the camera position in the world. More precisely the vector **t** defines the position of the world origin in the camera coordinates whereas the columns of R are the director cosines of the world-axes in camera coordinates.

In order to extract the 2D coordinates a laser probe with a green tip has been integrated to the Micron and then used to scan the surface (Fig. A.2). The mapping between the tracking system (ASAP) and the camera plane is obtained through the fundamental perspective camera equation:

$$x_{tip} = PX_{tip}^{ASAP} \tag{A.1}$$

where $x_{tip} \in \mathbb{R}$ is a 3x1 vector defining the 2D location of the tool tip in homogeneous coordinates, $X_{tip}^{ASAP} \in \mathbb{R}$ is a 4x1 vector representing the 3D location of the tool tip in homogeneous coordinates and P is the 3x4 camera matrix. Each camera is characterized by its own projection matrix that can be retrieved given the world coordinates of a set of

$$P = \overbrace{K}^{\text{Intrinsic Matrix}} \times \overbrace{[R \mid \mathbf{t}]}^{\text{Extrinsic Matrix}}$$

$$= \overbrace{\underbrace{\begin{pmatrix} 1 & 0 & x_0 \\ 0 & 1 & y_0 \\ 0 & 0 & 1 \end{pmatrix}}_{\text{2D Translation}} \times \underbrace{\begin{pmatrix} f_x & 0 & 0 \\ 0 & f_y & 0 \\ 0 & 0 & 1 \end{pmatrix}}_{\text{2D Scaling}} \times \underbrace{\begin{pmatrix} 1 & s/f_x & 0 \\ 0 & 1 & 0 \\ 0 & 0 & 1 \end{pmatrix}}_{\text{2D Shear}}}^{\text{Intrinsic Matrix}} \times \overbrace{\underbrace{\left(\begin{array}{c|c} I & \mathbf{t} \end{array} \right)}_{\text{3D Translation}} \times \underbrace{\left(\begin{array}{c|c} R & 0 \\ \hline 0 & 1 \end{array} \right)}_{\text{3D Rotation}}}^{\text{Extrinsic Matrix}}$$

Figure A.1: The camera projection matrix mapping the 3D position of a point expressed in homogeneous coordinates in the 2D image reference frame. It is the result of 5 transformations: a 2D translation, a 2D scaling, a 2D shear, a 3D translation and a 3D rotation. x_0 and y_0 are the offset coordinates of the principal point. f_x and f_y refer to the focal length. s is the axis skew. R and **t** are respectively the rotation matrix and the translation vector that describe the camera position in the world.

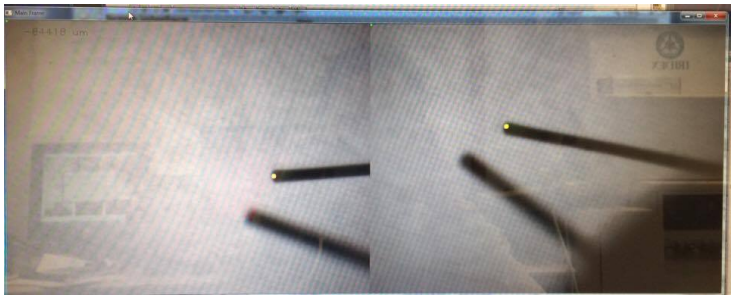

Figure A.2: Calibration procedure. A laser probe integrated into the Micron tool is scanned over a white surface and the position of its green tip is extracted.

point X_i and the corresponding 2D coordinates of the same set x_i. The system of equation is defined as:

$$x_{i1} = PX_i \quad and \quad x_{i2} = P'X_i \tag{A.2}$$

We can obtain the camera calibration using the Direct Linear Transformation (DLT) method [28]. Calibration is accomplished on-line extracting the necessary information in a 5-60 s video sequences moving the tool in random positions through the workspace. In one minute of acquisition it is possible to extract roughly 2000 data points. The quality of the registration is affected by the accuracy of the 3D tip location which is not directly measured but it is derived from the LEDs on the Micron moving platform. Theoretically the tool offset T_{offset} could be used to define the tip coordinates exploiting the following rigid body transformation and the position and orientation of the moving platform P_{wt}:

$$X_{tip}^{ASAP} \equiv P_{wt}T_{offset} \tag{A.3}$$

However, this method can lead to significant errors because the pose estimation is influenced by any kind of lateral deflections of the tip. Hence, another solution has been proposed in order to determine the tip offset considering the projection error of the tool tip in images. The projection error increases under big variations of the tool orientation while moving the Micron over the surface. The tip offsets are computed considering the tool length l_0 and the angular variations along x and y θ_x and θ_y:

$$T_{offset} \equiv R_x(\theta_x) \cdot R_y(\theta_y) \cdot T_0, \quad T_0 = [0 \quad 0 \quad l_0 \quad 1]^T \tag{A.4}$$

The squared sum of the projection errors in the left and the right camera is minimized according to the optimization method:

$$\min(\sum_{i=1}^{n} \left[(p_{projL}^i - p_{DetL}^i)^2 + (p_{projR}^i - p_{DetR}^i)^2 \right]) \tag{A.5}$$

where p_{projL}^i and p_{projR}^i are the projections of the tool tip computed with the Eq. A.3 while p_{DetL}^i and p_{DetR}^i are the detected tip positions. The algorithm computes the offset through an unconstrained nonlinear optimization. Thus, the camera matrices are extracted applying an optimization technique that relies on the value the projection errors in order to simultaneously find the tool offset and the camera matrices.

Appendix B

Triangulation Given P and P', the camera projections matrices obtained with the camera calibration, we can express the corresponding points as:

$$PX_i = x_i \quad and \quad P'X_i = x'_i \tag{B.1}$$

The triangulation operation and the metric 3D geometry allow to determine the location of the points X_i in the 3D world. Indeed, since the camera matrices are known it is possible to extract viewing rays in the camera reference system, the position and orientation of rays from both camera in the 3D space. Since each point in the image is a line in the 3D world in the ideal case X is found as the intersection of two 3D rays: the ray from $\hat{x}$ passing through the focal point O and the ray from $\hat{x}'$ through O' (Fig.B.1a). In practice the lines generated by the matching points do not intersect due to a combination of factors such as geometric noise from calibration parameters (Fig.B.1b). Geometric distorsion such as lens distorsion is due to the deviation of the 2D-3D mapping from the pinhole camera model. An other factor is the image representation based on point spread functions that cause ray dispersions in the lens system. In addition for digital cameras the interpolation of a discrete intensity function must be applied to extract 2D points location. Thus, the coordinates of the points on the image planes cannot be measured precisely and this inaccuracy leads necessarily to errors in the triangulation. Thus, we can just find an optimal 3D point, a "pseudo-intersection point" that can be retrieved in different ways applying the SSD to both rays (mid-point method). Given d(L,X), the Euclidean distance between a 3D line and a 3D point and the projection lines L_1'and L_2', the mid-point method works

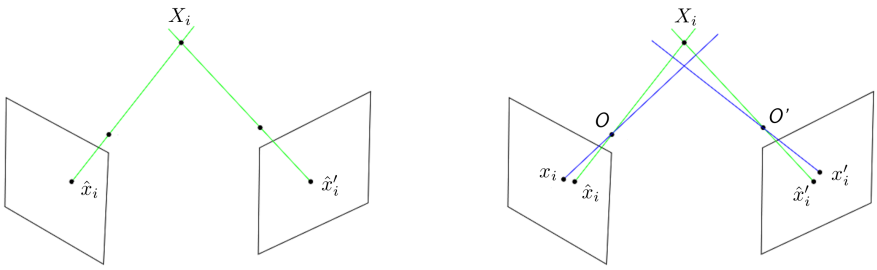

(a) **(b)**

Figure B.1: Triangulation method.(a) In the ideal case of epipolar geometry the projections of the 3D point ($\hat{x_i}$ and $\hat{x'_i}$) into the image planes are obtained tracing a line that passes through the focal points O and O'. (b) In practice the positions of points $\hat{x_i}$ and $\hat{x_i}$" cannot be measured with arbitrary accuracy but x_i and x'_i are used for the 3D reconstruction so the projection lines may not have any point in common.

on the minimization of:

$$d(L'_1, X)^2 + d(L'_2, X)^2 \tag{B.2}$$

The solution x corresponds exactly on the mid-point of the shortest segment that connects the two projection line.

Appendix C

Convex hull implementation Given S, a set of point coordinates, the convex hull C(s) is found as the smallest convex set that encompasses S. The convex hull is modeled as a triangular mesh whose vertices are points of the dataset S [25]. The 3D convex hull is represented by a set of vertices and 2-dimensional faces, the facets. Each point of S that is also a convex hull's vertex is called extreme vertex. The ridge is the boundary element that two adjacent facets share. In R3 the facets are modeled as triangles and the ridges as edges.

The Quickhull algorithm, relies on the incremental recursive insertion method. The convexhull is retrieved adding iteratively an input point outside the volume that is initialized as a 4-vertices tetrahedron. After initialization, each unprocessed point is attributed to an outside set referred to a facet. At each iteration the algorithm rejects every point found to be inside the volume and it includes the point found to be more distant from the volume's facets. The partitioning operation determines a new visible facet for every point at each iteration since every time a point is included, the Quickhull produces new facets and new outside sets. Partitioning allows to compute the furthest point of each outside set and the points below the new facets that have to be rejected. It stops as soon as the last point outside the volume has been added. In order to determine whereas a point belongs to the outside set of the facets or not the Quickhull deals with the concept of hyperplane which is defined by its outward-pointing unit normal and the origin offset. The signed distance to hyperplane is a geometrical parameter that is computed as the inner product

between the point and the normal plus the offset. If this value is positive the unassigned point lies above the hyperplane and it is assigned to the facet's outside set. If an unprocessed point lies above two or more facets, the choice of the outside set is irrelevant because at the next step of the algorithm it will be added to the volume anyway.